Quantitative tools for seismic stratigraphy and lithology characterization

Felix Herrmann, ERL, MIT

Abstract

Seismological images represent maps of the earth's structure. Apparent bandwidth limitation of seismic data prevents successful estimation of transition sharpness by the multiscale wavelet transform. We discuss the application of two recently developed techniques for (non-linear) singularity analysis designed for bandwidth limited data, such as imaged seismic reflectivity.

The first method is a generalization of Mallat's *modulus maxima* approach to a method capable of estimating coarse-grained local scaling/sharpness/Hölder regularity of edges/transitions from data residing at essentially one single scale. The method is based on a non-linear criterion predicting the (dis)appearance of local maxima as a function of the data's fractional integrations/differentiations.

The second method is an extension of an atomic decomposition technique based on the greedy Matching Pursuit Algorithm. Instead of the ordinary Spline Wavelet Packet Basis, our method uses multiple Fractional Spline Wavelet Packet Bases, especially designed for seismic reflectivity data. The first method excels in pinpointing the location of the singularities (the stratigraphy). The second method improves the singularity characterization by providing information on the transition's location, magnitude, scale, order and direction (anti-/causal/symmetric). Moreover, the atomic decomposition entails data compression, denoising and deconvolution.

The output of both methods produces a map of the earth's singularity structure. These maps can be overlayed with seismic data, thus providing us with a means to more precisely characterize the seismic reflectivity's litho-stratigraphical information content.

1 Introduction

Localized detection and characterization of singularities is an important step in the analysis of various signals and images. Within the geosciences, signals and images in particular, contain a wide variety of singularities and edges. The presence of these singularities results in stochastic non-stationarity of the data, limiting the applicability of conventional techniques, which often rely on stationarity assumptions.

For broadband signals, multifractal analysis, based on the wavelet transform, has been applied successfully to globally characterize the singularity structure, i.e. the structure of "non-stationarities", by means of the singularity spectrum (Bacry et al., 1993; Jaffard, 1997a; Herrmann, 1997, 1998b, 2000). Estimates for the singularity spectrum suggest that the observed data may be considered as a sampled multifractal function (Jaffard, 1997a), with an accumulation of singularities.

In seismology, the usefulness of the multifractal framework is limited because information on the local singularity structure characteristics is lost. Results by Holschneider (1995); Mallat (1997) and Jaffard and Meyer (1996) show that local Hölder exponents can be estimated from the localized decay/growth rate of the wavelet coefficients, along the wavelet transform *modulus maxima* lines (Mallat, 1997; Jaffard, 1997a; Herrmann, 1997, 1998b). Unfortunately, these techniques also suffer from the bandwidth limitation and singularity "accumulation". Seismic waves, for example, observe the multifractal earth (Herrmann, 1997, 1998b) at the scale of only one wavelet because seismic waves, as are many other remotely sensed data, are bandwidth limited.

Both accumulation and bandwidth limitation prevent a useful characterization of the local sharpness/regularity by scale exponents. For reflectors this sharpness measures the abruptness of transitions and is able to answer questions such as does this transition look like a jump discontinuity, a ramp function or a "thin" layer?

To tackle the bandwidth limitation problem two different analysis methods are proposed. The first method is valid under particular conditions on the data, and locally detects and characterizes singularity

strengths from both well-log and imaged reflectivity (Herrmann and Stark, 1999, 2000, 2001; Herrmann et al., 2000), using a non-linear amplitude independent criterion. The method amounts to a generalization of the continuous wavelet transform (CWT) to a transform where the "wavelets" are fractional integro-differentiations of the Gaussian bell shape. By varying the order of the wavelets for a fixed scale, coarse-grained scale exponents are found via the creation or removal of local *modulus maxima* as a function of the order. In the small-scale limit these exponents are equivalent to Hölder exponents, as shown by Zähle (1995), who also applies fractional calculus to regularity estimation. Given these estimates we are not only able to check well and seismic data for litho-statigrapical content, but we are also able to generate reconstructions.

The second method we propose sacrifices some of the amplitude insensitivity of the first method in favor of more mathematical rigor, near perfect reconstruction and additional stratigraphical information, such as the characteristic length scale and direction. The method is based on Fractional Splines Wavelets (Unser and Blu, 2000; Blu and Unser, 2000), which are used to span a redundant dictionary defined by a multitude of Fractonal Spline Wavelet Packet Bases (Coifman et al., 1992; Mallat, 1997). This dictionary is used to decompose the data into a limited number of atoms, using a "greedy" non-linear Matching Pursuit Algorithm (Mallat, 1997). This greedy algorithm searches data for coherent structures, which by our dictionary design are optimally adapted to the behavior of reflection events. The selection procedure of Atomic Decomposition schemes is based on a correlation measure between atoms and events in the data. Therefore, the method is able not only to optimally (read sparsely) represent the data, but also also provides an estimation procedure for local scaling information.

Both applied methods explore the property that, to leading order, relative changes in seismic reflection signatures carry information on the local scaling characteristics of geological boundaries. As shown by Muller et al. (1992) and later by Herrmann (1997) sedimentary records consist of a wide variety of transitions, which not only differ in sharpness (Herrmann, 2001) but also in characteristic length scale and direction. Inherent bandwidth limitation of seismic data and the presence of many closed spaced transitions make it difficult to characterize these different types of transitions.

Attempts by Harms and Tackenberg (1972) and Payton (1977) to characterize geological transitions date back from as early as the late 70's and early 80's, during which seismic stratigraphical methods were proposed, based on instantaneous phase behavior of seismic waves. In these approaches, the litho-stratigrapical boundaries are typically described by sub-wavelength combinations of jump and/or first order discontinuities, reflecting particular types of depositional environments, i.e. sorting of the sands. Because these different transitions yield a particular phase behavior, the instantaneous phase provides a natural vehicle to distinguish between different facies types. Initially, instantaneous phase was computed by complex trace analysis, based on an analytic continuation of the seismic response function using the Hilbert transform. Despite their success, the original complex trace attributes had the disadvantage to (1) be based on the non-local Hilbert transform; (2) be sensitive to noise; and (3) be "noisy" in cases where the reflection data contain many "fluctuations". Also, the effectiveness of the original transition parametization is limited since it relies on a sub-wavelength characterization (Payton, 1977; Verhelst, 2000), which requires information unattainable from bandwidth limited seismic data.

By generalizing zero (jump) or first order (ramp) transitions to fractional order transitions, Herrmann (1997); Herrmann and Stark (2000), and later Dessing (1997) were able to locally characterize transitions (singularities) by a single order/scale exponent, describing the scaling, sharpness and phase properties of abrupt changes in the elastic properties. While Dessing (1997) and Verhelst (2000) resort to the complex wavelet transform and Gabor Atom Matching Pursuit algorithm, to estimate the scale exponent (Dessing, 1997) and phase-scale information (Verhelst, 2000), Herrmann (2001) proposed two alternative monoscale methods to find the location and transition orders from bandwidth limited data (see also Lyons and Herrmann in this report). Both methods derive their basis from a generalization of the traditional jump discontinuity model to a model with fractional order transitions. The first method employs specific properties of integro-differentials of these generalized transitions, whereas Unser and Blu (2000)'s Fractional Splines derive their existence from a similar generalization within the framework of Splines and Spline Wavelets.

The primary goals of this paper are: (1) to establish a direct link between the wavelet transform and seismic reflectivity; (2) to introduce a new measure, which expresses local orders of magnitude for variations in both the medium and wavefield; and (3) to present two analysis methods, respectively, based on fractional order continuous wavelet transforms and Fractional Spline Wavelet Packet dictionaries, both of which estimate singularity orders at more or less a fixed scale. Attempts to estimate the local scale exponents at a fixed scale have also been made by Dessing (1997) and Struzik (2000).

The paper is organized as follows. First, we present a review on the essentials of the seismic method

in the simplified case where the medium is considered to vary along the vertical only. For small medium variations, the forward and inverse mappings of the medium properties to the seismic wavefield and back are linearized and written in terms of temporal and spatial convolutions. Next, we demonstrate the relation of these convolutions to particular instances of limited scale range continuous wavelet transforms of the medium fluctuations. In section 4, we introduce the first method to detect and characterize singularities at essentially the fixed scale of the seismic wavelet. Given the singularity characterization, singularity maps of the earth are generated. These maps are used for the interpetation and reconstruction of pseudo-medium profiles and reflectivity images. Section 5 contains an exposition of the atomic decomposition, where Fractional Splines are introduced, followed by the definition of Fractional Spline Wavelets, Wavelet Packet Transforms and Atomic Decompositions and their related properties, such as convergence, denoising and deconvolution. Finally, in Section 6, we present a litho-stratigrapical boundary facies characterization based on singularity characterization, obtained by the two analyzing methods.

2 Seismic reflectivity imaging method

In the seismic reflection method, recorded surface reflectivity data are converted to an image of the earth's subsurface structure through a process called "migration". Seismic data itself consists of measurements of the wavefield, acquired by geo/hydrophones, which measure the earth's response to a source located at the surface. The process of pre-stack depth migration (Gardner, 1985; Berkhout, 1987) is based on a time-reversed map of the recorded surface seismic data to a depth-parametrized, reflectivity function. The time-reversal operators are obtained by solving a linear wave equation for the up- and downward wave constituents, and require *a priori* knowledge of the smooth part of the velocity structure. By applying time-reversal operators to the data, information is obtained on the singularities in the earth's medium properties. This information is contained in the reflection density function. When performed correctly, i.e. when the *a priori* velocity information is accurate enough, migration operators are pseudo-differential, mapping the singularities one to one, from the recorded seismic data to the imaged reflectivity function (Symes, 1995; de Hoop and Bleistein, 1997). For the purpose of this paper it suffices to consider acoustic media, which vary along the vertical coordinate only. First, the one-way representation for the forward and inverse maps will be presented, followed by a linearization in terms of small medium variations.

2.1 The forward map: one-way wavefield representation

Medium variations of the earth exhibit a distinct directional preference along the vertical. Therefore, a formulation in terms of a one-way wave equation is beneficial. This formulation distinguishes between up- and downward traveling waves. As a consequence, natural separation can be made between the propagation and reflection of seismic waves. Following Berkhout (1987); Wapenaar and Berkhout (1989); Wapenaar (1996); Grimbergen et al. (1998); de Hoop (1992, 1998) and Wapenaar et al. (1999), we can write, for acoustic one-dimensional media, the upgoing acoustic pressure at the surface ($z = 0$) as

$$\hat{p}(\mathrm{p}, z = 0; \omega) = \int_{z=0}^{\infty} \hat{w}^{-}(\mathrm{p}, 0, z; \omega) r(\mathrm{p}, z) \hat{w}^{+}(\mathrm{p}, z, 0; \omega) \hat{\varphi}(\omega) \mathrm{d}z. \tag{1}$$

In the above temporal frequency ray-parameter (p, ω)-domain formulation:

- Symbol $\hat{}$ indicates temporal Fourier transformed quantities, i.e. $\hat{f}(\omega) = \mathcal{F}\{f\}(\omega)$, with the inverse Fourier transform $f(t) = \mathcal{F}^{-1}\{\hat{f}\}(t)$ and where t stands for the intercept time.
- z is the vertical coordinate (positive z-direction points downward), $\mathrm{p} = \frac{\sin\theta(z)}{c(z)}$ the ray-parameter with θ the angle of incidence and $c(z)$ the depth-dependent wavespeed, and $\omega = 2\pi f$ the temporal angular frequency.
- $\hat{p}(\mathrm{p}, z = 0; \omega)$ represents the decomposed plane-wave reflection data at the surface, i.e. a monochromatic plane upward-traveling pressure wave.
- $\hat{w}^{+}(\mathrm{p}, z, 0; \omega)$ and $\hat{w}^{-}(\mathrm{p}, 0, z; \omega)$ are the flux-normalized single-scatter propagation operators given by

$$\hat{w}^{+}(\mathrm{p}, z, 0; \omega) = \hat{w}^{-}(\mathrm{p}, 0, z; \omega) = \exp[j\omega \int_{0}^{z} q(\mathrm{p}, z')\mathrm{d}z'], \tag{2}$$

  with $q(\mathrm{p}, z) = \sqrt{\frac{1}{c^2(z)} - \mathrm{p}^2}$ the local vertical slowness.

- $r(\mathrm{p}, z)$ is the p-dependent reflection density,

$$r(\mathrm{p}, z) = \frac{1}{2Y}\partial_z Y(\mathrm{p}, z) \quad \text{with} \quad Y(\mathrm{p}, z) = q(\mathrm{p}, z)/\rho(z) \tag{3}$$

  with $Y(\mathrm{p}, z)$ the acoustic admittance and $\rho(z)$ the volume density of mass.

- $\hat{\varphi}(\omega)$ represents the frequency characteristics of a bandwidth-limited downward source function.

The propagation operators carry the source wavefield from the surface down to the reflector and back up to a detector at the surface. The reflection density couples the down- and upward traveling waves at depth levels where the acoustic admittance varies. The one-way wavefield representation of Eq. 1 is approximate because it is based on the first term in the Bremmer series expansion (de Hoop, 1998), yielding single scattered waves only.

Despite the approximation, Eq. 1 captures leading order terms, describing the forward mapping of the medium singularities to the wavefield. For a constant background velocity model ($\bar{c} =$ constant), Eq. 1 can be written as a temporal convolution:

$$p(\mathrm{p}, z=0; t) = \left(r_t(\mathrm{p}, \cdot) *_t \varphi\right)(\mathrm{p}; t) \quad \text{with} \quad r_t(\mathrm{p}, t) = \frac{1}{2\bar{q}(\mathrm{p})} r(\mathrm{p}, \frac{t}{2\bar{q}(\mathrm{p})}), \tag{4}$$

where $*_t$, denotes time convolution. The $r_t(\mathrm{p}, t)$ represents the depth to two-way traveltime-converted reflection density. Eq. 4 defines after linearization the functional form for the forward map, which describes how the medium variations are mapped to the wavefield.

2.2 The inverse map: migration and stacking

After applying the downward extrapolation with time-reversed extrapolation operators (de Hoop, 1998) and neglecting multiple scattering we find by imposing the imaging condition, the following expression for the imaged reflectivity (Wapenaar et al., 1999):

$$\langle R(\mathrm{p}, z)\rangle = \frac{2\bar{q}(\mathrm{p})}{\pi} \Re \int_0^\infty \hat{p}(\mathrm{p}, z; \omega) \mathrm{d}\omega. \tag{5}$$

In this expression the imaged reflectivity equals the downward continued pressure wavefield evaluated at time zero, $\langle R(\mathrm{p}, z)\rangle \triangleq p(\mathrm{p}, z; t=0)$ with $p(\mathrm{p}, z; t)$ the inverse Fourier transformed downward continued pressure. Eq. 5 contains the source contribution and the angular brackets $\langle\,\rangle$ are used to denote the resulting bandwidth limitation.

Likewise, the surface reflectivity – the imaged reflectivity (cf. Eq. 5) – can also be formulated as a convolution. Substitution of Eq. 5 into the one-way wave representation (cf. Eq. 1) yields,

$$\langle R(\mathrm{p}, z)\rangle = \frac{2\bar{q}(\mathrm{p})}{\pi} (r_+(\mathrm{p}, \cdot) *_z \varphi_z)(\mathrm{p}, z), \tag{6}$$

where $*_z$ denotes depth convolution. The source function and reflection density are now given by

$$\varphi_z(\mathrm{p}, z) = \varphi(\cdot 2\bar{q}(\mathrm{p}))(z) \quad \text{and} \quad r_+(\mathrm{p}, \cdot) = H(z - \cdot) r(\mathrm{p}, \cdot), \tag{7}$$

with $H(\cdot)$ the Heaviside distribution. Equation 7 corresponds to a p-dependent rescaling of the temporal source function. To complete the inverse map that relates the surface reflectivity back to the medium properties, we propose the following simplified stacking:

$$\langle \boldsymbol{\Delta}(z)\rangle = \int_{\mathrm{p}_0}^{\mathrm{p}_1} \langle R(\mathrm{p}, z)\rangle \mathrm{d}\mathrm{p}. \tag{8}$$

Compared to commonly used stacking, Eq. 8 neglects frequency weighting normally found in the inverse Radon transform. Later, this choice will allow us to identify stacking as an inverse wavelet transform of the medium. Eq.'s 6 and 8 combined form the basis for the inverse map. Both expressions for the forward and inverse maps are still non-linear in the medium properties. In the next section, we will linearize the expression for reflection density.

2.3 Linearized forward and inverse maps

Following Ostrander (1994); Catagna and Backus (1993) and van Wijngaarden (1998), the reflection density can be linearized in the normalized acoustic impedance ($\Delta Z(z)$) and compressional wavespeed (Δc) fluctuations, yielding,

$$r(\mathrm{p},z) \approx \left[\frac{1}{2} \quad \frac{1}{2}\frac{\bar{c}^2\mathrm{p}^2}{\cos\bar{\theta}(\mathrm{p})}\right]\partial_z\left[\Delta Z \quad \Delta c\right]^T = \bar{\mathbf{M}}(\mathrm{p})\partial_z\mathbf{\Delta}(z). \tag{9}$$

Here, $\cos\bar{\theta}(\mathrm{p}) = \sqrt{1-\bar{c}^2\mathrm{p}^2}$ and $\Delta Z \approx \Delta c + \Delta\rho$. This expression is linear in the normalized medium fluctuations. These fluctuations are assumed to be small and given by $\Delta f(z) = \frac{f(z)-\bar{f}}{\bar{f}} \ll 1$ with $f(z)$ and $\bar{f}(z)$ being either the actual/background acoustic impedance or the actual/background wavespeeds. Notice that the p-dependent factor of Eq. 9 remains non-linear in the background velocity, $\bar{c}$.

Given the linearized expression for the reflection density, we are able to derive linear functionals for forward mapping, imaging step and inverse mapping. Using Eq.'s 4 and 9 we find

$$p(\mathrm{p},z=0;t) \approx \mathbf{L}\{\bar{c};\mathbf{\Delta},\varphi\}(\mathrm{p},t) = \frac{\bar{\mathbf{M}}(\mathrm{p})}{2\bar{q}}(\mathrm{p})(\partial_t\mathbf{\Delta}(\frac{\cdot}{2\bar{q}(\mathrm{p})}) *_t \varphi)(t), \tag{10}$$

for the approximate linearized forward map ($\mathbf{L}\{\bar{c};\mathbf{\Delta},\varphi\}$). This forward map depends on the seismic wavelet and linearly maps the medium fluctuations to variations in the pressure wavefield. After imaging, we obtain a similar expression

$$\langle R\rangle(\mathrm{p},z) = \frac{2\bar{q}(\mathrm{p})}{\pi}\bar{\mathbf{M}}(\mathrm{p})(\partial_z\mathbf{\Delta}_+ *_z \phi_z)(z), \tag{11}$$

for the imaged reflectivity. Finally, after stacking, the inverse mapping equals

$$\langle\mathbf{\Delta}\rangle(z) = \mathbf{L}^*\{\bar{c};\langle R\rangle\}(z) = \left(\mathbf{L}^*\circ\mathbf{L}\right)(z) \approx \int_{\mathrm{p}_0}^{\mathrm{p}_1}\langle R\rangle(\mathrm{p},z)\mathrm{dp}, \tag{12}$$

where $\mathbf{L}^*$ refers to the approximate formal adjoint (Symes, 1995) of the one-way forward map $\mathbf{L}$ and $\circ$ denotes functional composition. Depending on the application, the inverse mapping can be supplemented with an additional pre- or post-stack deconvolution for the source wavelet.

Both linearized maps in Eq.'s 10 and 12 describe the reflection and subsequent imaging and inversion to leading order. Following Symes (1995), one can show that the operator $\left(\mathbf{L}^*\circ\mathbf{L}\right)(z)$ is approximately pseudo-differential when the reference velocity model ($\bar{c}(z)$) is close enough to the smooth part of the actual velocity model. Consequently, singularities in the acoustic medium are preserved during the seismic "acquisition process" ($\mathbf{L}$) and processing ($\mathbf{L}^*$). During processing, migration primarily concerns itself with finding the *locii* of the singularities, whereas during inversion, information on the magnitude of the acoustic medium variations are targeted.

Despite significant progress in migration and inversion (Symes, 1995; de Hoop, 1996), acquiring information on the actual medium fluctuations remains difficult. Primary reasons are (1) the requirement of true amplitude data, not necessarily met in the field; (2) the lack of an accurate velocity reference model; and (3) the theoretical requirement of a *separation of scales*, underlying the wave theoretical formulation (Symes, 1995). These difficulties form the primary motivation for this paper, where we will direct our attention towards finding the *locii* and orders of singularities instead of inverting for actual medium properties. Since the operators are approximately pseudo-differential, we may expect the singularity orders to represent a robust quantity during the seismic data processing flow. In the next section, we explore relationships between the forward/inverse maps and the forward and inverse wavelet transform.

3 Wavelets and seismic reflectivity

Singular functions with isolated (Holschneider, 1995; Mallat, 1997; Jaffard and Meyer, 1996) or accumulated (Bacry et al., 1993; Holschneider, 1995; Jaffard and Meyer, 1996; Jaffard, 1997a,b; Mallat, 1997; Jaffard, 1997a,b) singularities have successfully been analyzed by the continuous wavelet transform (CWT). The singularities in these functions refer to edges/transitions in the medium properties (Herrmann, 1997, 1998b; Herrmann and Stark, 2001; Herrmann et al., 2000; Herrmann, 2000) and to singularities in the wavefront set (Herrmann and Stark, 2001; Herrmann et al., 2000; Herrmann, 2000). For isolated singularities, Hölder/Lipschitz exponents can be assigned to locally describe the regularity. Global regularity information is obtained by multifractal analysis, which produces a global but useful characterization,

containing information on relationships between Besov norms of the medium and reflectivity (Herrmann, 2000).

As shown by Muller et al. (1992); Saucier and Muller (1993); Herrmann (1997) and Herrmann (1998b, 2000), well-log data, as well as seismic reflectivity (Herrmann, 1997, 1998b, 2000) behave multifractally which means that they display heterogeneous scaling behavior. Well-log data are *in situ* measurements of the earth subsurface, taken with a tool that is lowered into the borehole. The scaling heterogeneity means that the medium behaves as

$$|f(z+\Delta)-f(z)| \leq C\Delta^{\alpha(z)} \quad \text{as} \quad \Delta \to 0, \tag{13}$$

where C is a finite constant and α the depth dependent Lipschitz/Hölder exponent. These exponents vary discontinuously (Riedi et al., 1998), an indication of multifractality.

First, we introduce the continuous wavelet transform, followed by techniques to locally detect, measure and characterize singularities. Then, a direct link between seismic reflectivity and the wavelet transform will be established. Finally, a generalized transition model will be presented, yielding an effective parameterization by means of homogeneous distributions (Gel'fand and Shilov, 1964; Zemanian, 1965; Holschneider, 1995), which go beyond the commonly used zero or first order discontinuities (Herrmann, 1997, 1998b; Herrmann et al., 2000; Herrmann, 2000).

3.1 The continuous wavelet transform

Multiscale analysis by the continuous wavelet transform (CWT) can be seen as the interplay of a *smoothing* and a *de-smoothing* operation. This property becomes apparent when we define the CWT (Mallat, 1997) as a multiscale derivative operator acting on the function f,

$$\mathcal{W}\{f,\psi^M\}(\sigma,z) \triangleq \overbrace{\sigma^M \frac{\mathrm{d}^M}{\mathrm{d}z^M} \underbrace{(f*\phi_\sigma)(z)}_{\text{smoothing}}}^{\text{de-smoothing}} = (f*\psi_\sigma^{(M)})(z). \tag{14}$$

In this expression, $\mathcal{W}\{f,\psi^M\}(\sigma,z)$ denote the wavelet coefficients of f with $\psi_\sigma^{(M)}$ the M^{th}-order scale-indexed analyzing wavelets. We define the wavelets as derivatives of dilated, real and symmetric smoothing functions ($\phi_\sigma(z)$):

$$\phi_\sigma(z) \triangleq \frac{1}{\sigma}\phi(\frac{z}{\sigma}) \quad \text{and} \quad \psi_\sigma^M(z) = (-1)^M \sigma^M \frac{\mathrm{d}^M}{\mathrm{d}z^M}\phi_\sigma(z). \tag{15}$$

The wavelets are L^1-normalized and have an effective support proportional to the scale σ, which is related to the reciprocal of the dominant wavenumber, $\sigma \sim 1/\zeta_0$.

For the specific case of a Gaussian bell-shape smoothing function and $M=2$, the wavelet $\psi_\sigma^2(z)$ becomes a Ricker wavelet, also known as a Mexican hat. Now, the wavelet transform of Eq. 14 can be written as (Holschneider, 1995):

$$\mathcal{W}\{f,\psi^2\}(\sigma,z) \triangleq -\sigma\frac{\mathrm{d}}{\mathrm{d}\sigma}(f*\phi_\sigma)(z), \tag{16}$$

yielding wavelet coefficients that are given by the $\log\sigma$-derivative of the smoothings. Notice that these smoothings contain *all* scales up to σ, while the wavelet coefficients contain only the *details* of f *at* σ.

By computing the inverse wavelet transform (ICWT, (Daubechies, 1992; Mallat and Hwang, 1992; Holschneider, 1995; Jaffard and Meyer, 1996; Mallat, 1997; Carmona et al., 1998)) defined as

$$f(z) = \int_0^\infty \int_{-\infty}^{+\infty} \mathcal{W}\{f,\psi\}(\sigma,z')\tilde{\psi}(\frac{z-z'}{\sigma})\mathrm{d}z'\frac{\mathrm{d}\sigma}{\sigma} \tag{17}$$

f can be reconstructed. In this inverse transform, the wavelet and its "dual", $\tilde{\psi}$, are related by $1 = \int_0^\infty \hat{\tilde{\psi}}(\zeta)\bar{\psi}(\zeta)\frac{\mathrm{d}\zeta}{\zeta}$ where $\bar{\cdot}$ is the complex conjugate. The reconstruction holds *modulo* polynomials when f is a tempered distribution, $f \in S'(\mathbb{R})$, e.g. f is a delta distribution. Under the restriction $1 = \int_0^\infty \bar{\hat{\psi}}(\sigma\zeta)\frac{\mathrm{d}\sigma}{\sigma}$ we can, following Carmona et al. (1998), derive a simpler reconstruction formula

$$f(z) = \int_0^\infty \mathcal{W}\{f,\psi\}(\sigma,z)\frac{\mathrm{d}\sigma}{\sigma}, \tag{18}$$

which is possible because of redundancy within the CWT.

3.2 Local singularity characterization by scale exponents

Using multiscale analysis, the singularity strength can be calculated by following the wavelet coefficients along modulus maxima lines as a function of the scale. The singularity strength is expressed by scale exponents, measuring the local Lipschitz/Hölder regularity (Holschneider, 1995; Jaffard and Meyer, 1996; Mallat, 1997). Wavelets with M vanishing moments,

$$\int_{-\infty}^{+\infty} z^m \psi^M(z)\mathrm{d}z = 0 \quad \text{for} \quad m \leq M \tag{19}$$

are "blind", that is, their coefficients vanish with respect to polynomials of order $M-1$. As a result, wavelets detect and characterize singularities in the M^{th}-order derivative of $f(z)$. The wavelet coefficients of a $n \leq M$ times differentiable function, $f(z)$, measure the remainder of the n^{th} order Taylor approximation of $f(z)$ around the point $z = z_0$, i.e.

$$\mathcal{W}\{f,\psi\}(\sigma, z_0) = \mathcal{W}\{\varepsilon,\psi\}(\sigma, z_0) \tag{20}$$

with the remainder

$$|\varepsilon(z)| = |f(z) - P_n(z)| \leq K|z - z_0|^\alpha. \tag{21}$$

Here, $P_n(z)$ is the $n = \lfloor\alpha\rfloor$-order polynomial approximation of f around the point $z = z_0$. The remainder equals the difference between f and its approximation. Hölder exponents, α, measure the order of magnitude for the remainder. A function is called local Lipschitz/Hölder regular when the above inequality holds for a finite constant K. For technical details refer to Holschneider (1995); Jaffard and Meyer (1996) and Mallat (1997).

Following Mallat (1997); Bacry et al. (1993), the local Hölder regularity can be measured by the asymptotic decay/growth rate for the modulus maxima of the wavelet transform,

$$|\mathcal{W}\{f,\psi\}(\sigma, z)| \leq A\sigma^\alpha \quad \text{for} \quad z = Z(\sigma) \quad \text{as} \quad \sigma \to 0 \tag{22}$$

with A a finite scale, independent constant. The asymptotic behavior is studied along wavelet transform modulus maxima WTMM, that lie within the cone of influence given by $|z - z_0| \leq C\sigma$ and with C being the wavelet's support. Wavelet transform modulus maxima lines (WTMML, with $z = Z(\sigma)$) are found by connecting a line within this cone between the maxima across the different scales. The WTMML's are defined by

$$Z(\sigma) = \{z : \partial_z \mathcal{W}\{f,\psi\}(\sigma, z) = 0\}. \tag{23}$$

At each scale the local maximum should be a strict local maximum in either the right or left neighborhood of $z = z_0$ (see also definition 4.1). These local maxima (Mallat and Hwang, 1992; Mallat, 1997) delineate the major points of interest within the scale plane from which the original function can be reconstructed.

3.3 Seismic reflectivity as the continuous wavelet transform

Given the expression for the CWT (cf. Eq. 14), can we establish a relationship between this transform and the (imaged) seismic reflectivity? Comparing Eq. 14 with expressions for reflectivity we can show that for $M = 1$ both the linearized reflectivity at the surface and the imaged reflectivity can be expressed in terms of wavelet transforms. By replacing the source function by an analyzing wavelet, $\varphi(\cdot) \mapsto \frac{1}{\sigma}\psi(\frac{\cdot}{\sigma})$, and using Holschneider (1995)'s scale-covariance relations, we find

$$p(\mathrm{p}, z=0; t) = \frac{\bar{\mathbf{M}}(\mathrm{p})}{\sigma 2\bar{q}(\mathrm{p})}\mathcal{W}\{\mathbf{\Delta},\psi\}(\frac{\sigma}{2\bar{q}(p)}, \frac{t}{2\bar{q}(\mathrm{p})}), \tag{24}$$

and

$$\langle R(\mathrm{p}, z)\rangle = \frac{\bar{\mathbf{M}}(\mathrm{p})}{\sigma}\mathcal{W}\{\mathbf{\Delta}_+,\psi\}(\frac{\sigma}{2\bar{q}(p)}, z). \tag{25}$$

For the reflected pressure wavefield (cf. Eq. 24), the response is identical to a CWT with rescalings for both the scale and time axis, while the imaged reflectivity (cf. Eq. 25) involves only a rescaling of the scale axis. Stacking of the imaged reflectivity can, by comparing Eq.'s 8 and 18, be associated with an inverse wavelet transform:

$$\langle\mathbf{\Delta}\rangle(z) \sim \mathcal{W}^{-1}\{\langle R(\mathrm{p}, z)\rangle, \delta\}(z), \tag{26}$$

where the integration runs over a non-linear p-dependent "scale".

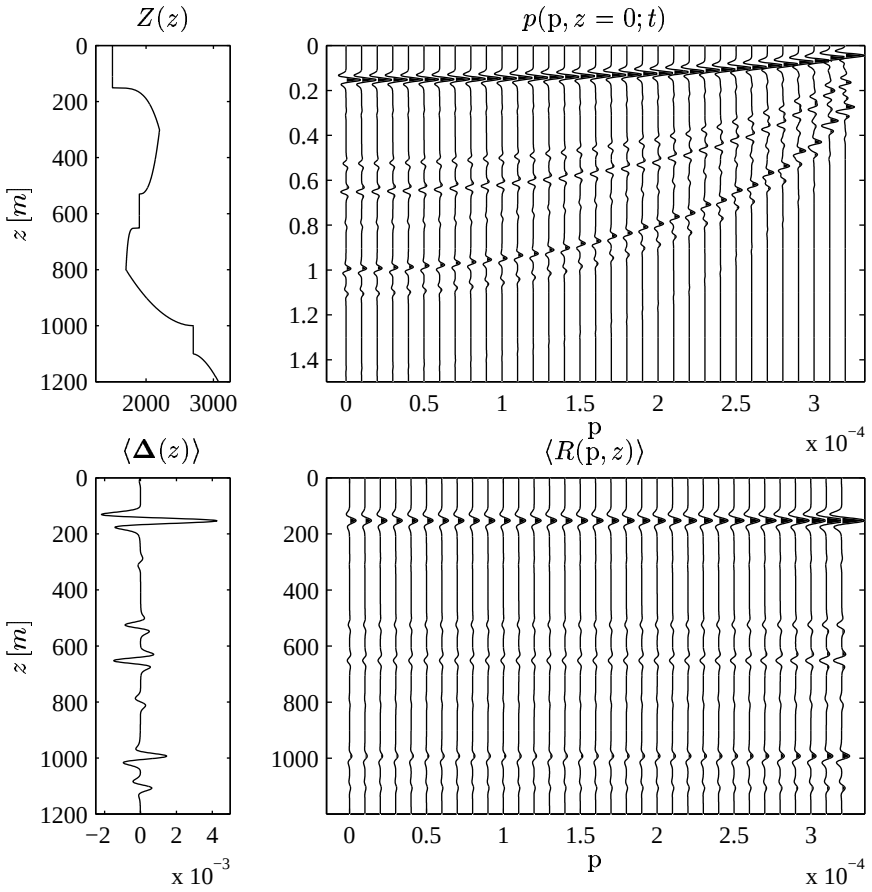

Figure 1: Illustration of the forward and inverse mappings (cf. Eq.'s 10 and 12) with a Ricker (Mexican hat) source function. Top (left): the acoustic impedance (c is kept constant); Top (right): the reflection data, $p(\mathrm{p}, z=0;t)$; Bottom (left): stacked imaged reflectivity; Bottom (right): imaged reflectivity, $\langle R(\mathrm{p},z)\rangle$. Notice the AVP in both reflectivities, the compression in time and dilation of the wavelet for the reflection data and the wavelet dilations for imaged reflectivity. Also notice the different signatures for the reflection events, preserved throughout the forward, inverse map and the stacking. Refer to section 3.4 for detail on how the transitions were defined.

Example 3.1 (Forward map)
Fig. 1 (top) contains the forward map of a medium profile with constant velocity and varying density. Top left, the acoustic impedance is plotted with five typical transitions (to be defined in section 3.4). Top right, the corresponding Radon-domain shot record, $p(\mathrm{p}, z=0;t)$, is displayed with the intercept time on the vertical and the ray-parameter on the horizontal axis. The source function is a Ricker wavelet (Mexican hat). Notice the time axis compressions and the wavelet dilations for the reflection data. Because the velocity is constant, the observed (AVP) behavior is caused solely by the scaling contribution (see Eq.'s 24-25). Also, notice the varying waveforms pertaining to the different reflectors. These different waveforms are also present in the pre-stack imaged reflectivity, depicted on the bottom right. In this plot, the reflections are aligned by the migration and a p*-dependent stretch may be observed. Finally, the stacked trace (bottom left) qualitatively confirms the partial reconstruction of the singularities in the medium fluctuations (cf. Eq. 26).*

From Eq.'s 24-26 and Example 3.1, we conclude that (i) amplitude *versus* ray-parameter (AVP)-behavior depends on both a *geometric* (by the $\mathbf{M}(\mathrm{p})$) and a *scaling* contribution (by the $\bar{q}(\mathrm{p})$ in the $\mathcal{W}$'s); (ii) waveforms are preserved (besides dilations); and (iii) singularities are partially reconstructed by stacking. These observations clearly suggest that seismic data contain information on the singularities in the

medium fluctuations. Even without source deconvolution, the stacking reconstructs the fluctuations for a scale range, limited by both the data's temporal frequency content and the available p-range.

3.4 Generalized reflector model: algebraic onset functions

When significant variations in the medium properties occur over length scales of the order of the seismic wavelength, waves are reflected. Correspondingly, wavelet coefficients are large at the location of singularities. Thus far, in seismology zero- or first-order discontinuities are mostly used to represent transitional regions in the earth's medium properties. Given the singularity detection and characterization capabilities of wavelets, why limit ourselves to these singularities? Why not consider the wider class of algebraic non-oscillatory singularities (Herrmann, 1997, 1998b,a; Herrmann and Stark, 2001; Herrmann et al., 2000) defined by

$$\chi_+^\alpha(z) \triangleq \begin{cases} 0 & z \le 0 \\ \frac{+z^\alpha}{\Gamma(\alpha+1)} & z > 0, \end{cases} \quad \text{and} \quad \chi_-^\alpha(z) \triangleq \begin{cases} \frac{-z^\alpha}{\Gamma(\alpha+1)} & z \le 0 \\ 0 & z > 0. \end{cases} \tag{27}$$

These singularities can be seen as building blocks of heterogeneously-scaling singular functions (cf. Eq. 13, (Bacry et al., 1993; Jaffard, 1997a)), and are used to define the medium variations as follows

$$f(z) = \bar{f}(z)[1 + \Delta f(z)] \quad \text{where} \quad \Delta f(z) = c_- \chi_-^\alpha(z - z_0) + c_+ \chi_+^\alpha(z - z_0). \tag{28}$$

Again, the barred quantity refers to a smoothly varying or constant function, while the fluctuations $\Delta f(z) \ll 1$ contain a generalized reflector, located at $z = z_0$. This reflector is given by a transition defined by the $\chi_-^\alpha(z)$ and $\chi_+^\alpha(z)$-functions. These functions are known as the causal/anti-causal homogeneous distributions, or onset functions (Gel'fand and Shilov, 1964; Zemanian, 1965; Holschneider, 1995), and are parametrized by the singularity-order exponent $\alpha \in \mathbb{R}$. These onset functions constitute only the principal part of the asymptotic expansion found in Holschneider (1995), pg. 294. For $\alpha \in C$ the singularities become oscillatory, a case not being considered in this paper. The $c_\pm$'s define the real valued bounded magnitude of the generalized reflector.

For $\alpha \ge 1$ the onset functions are continuous and differentiable; for $0 < \alpha < 1$ they are continuous but non-differentiable; and for $-1 < \alpha \le 0$ they are discontinuous and non-differentiable. Finally, for $\alpha \le -1$ the functions are no longer locally integrable and become singular tempered distributions. Besides the local regularity, the order parameter α also rules the homogeneity property,

$$\chi_\pm^\alpha(\sigma z) = \sigma^\alpha \chi_\pm^\alpha(z) \quad \sigma > 0. \tag{29}$$

This homogeneity property expresses the scale-invariance of the onset functions after appropriate rescalings. Scale-invariance is reflected into the following re-normalization property for the wavelet coefficients

$$\mathcal{W}\{f, \psi\}(\sigma_0, z) = (\frac{\sigma_1}{\sigma_0})^\alpha \mathcal{W}\{f, \psi\}(\sigma_1, z), \tag{30}$$

where f is defined as in Eq. 28. As a result, differences in scale of observation are interchangeable with the magnitude of the transition. This ambiguity makes it difficult to issue precise statements on amplitudes without knowledge of the (seismic) wavelet.

When $f(z)$ is defined according to Eq. 28, the wavelet coefficients display a power-law behavior for their moduli along WTMML's and in the log-log plane. Using

$$\log|\mathcal{W}\{f, \psi\}(\sigma, z)| \le \log A + \alpha \log \sigma \quad \text{for} \quad z = Z(\sigma) \quad \text{as} \quad \sigma \to 0, \tag{31}$$

we invert for the order of the transition, α, by estimating the slope of the wavelet coefficients.

4 Monoscale analysis by a generalized *modulus maxima* formalism

Within (exploration) seismology, the data are always bandwidth limited due to a combination of the finite-frequency range of the source, aperture limitation and possible dispersion effects. Consequently, the lack of available scale range may impede the asymptotics required to characterize the scaling by a single-scale exponent α. As a result, asymptotic techniques attempting to fit power-law dependence

in the seismic data are not applicable. At this point, we may argue that the data do not provide adequate information on the singularities. However, the waveform variations observed in the idealized, but bandwidth limited examples of Fig. 1, suggest that reflection events contain regularity/sharpness information on the reflector (Herrmann and Stark, 2000, 2001; Herrmann et al., 2000).

As possible remedies for the apparent lack of information, Dessing (1997) and Struzik (2000) propose to either compute the instantaneous phase or the local derivative of the wavelet coefficients in the log-log plane. The former author limits himself to isolated singularities while the latter aims to estimate coarse-grained Hölder exponents for singularities by constraining the range of possible local slopes. In this way Struzik (2000) is able to extend his method to non-isolates singularities without suffering from instabilities, arising from vanishing wavelet coefficients caused by mutual inferences of singularities. Both methods have the disadvantage that they (i) have to examine all the WTMML's pertaining to a single singularity; and (ii) lack an on/off criterion to predict the presence of a coarse-grained singularity.

To overcome some of these issues, a monoscale analysis method is introduced where the order of the wavelet is adapted to the singularity. The method is based on the heuristic that for the particular choice of singular functions as defined in Eq. 28, occurrences of modulus maxima depend on the wavelet order. By fractionally varying the amount of sharpening or de-sharpening in Eq. 14, we will examine the properties of convolution with a series of "wavelets"[1] consisting of fractional integro-differentiations of the Gaussian bell-shape smoothing function. Even though the Gaussian is not of compact support, it has, for integer[2] order moments, the advantage of propagating the maxima correctly towards the finer scales Mallat (1997).

First, we introduce a framework to calculate the fractional integro-differentiations, followed by the definition of a transformation with respect to fractional integro-differential orders of the Gaussian. Second, we devise a criterion that estimates, for a particular subclass of functions, the local coarse grained scale exponents as a function of causal/anti-causal fractional integro-differentiations. Finally, we present a simple reconstruction scheme that reconstructs the singularity structure of the original function, using the location, direction, local order, sign and magnitude of the singularities.

4.1 Fractional calculus

Following Zähle (1995); Gorenflo (1997); Unser and Blu (2000), let us define Liouville's generalization of differentiation of fractional orders as the left inverse of the action of the onset functions, as defined in Eq. 27. The causal fractional α^{th} derivative is defined according to

$$\left(\mathcal{D}_+^\alpha f\right)(z) \triangleq \left(\mathcal{D}^m \mathcal{I}_+^{m-\alpha} f\right)(z), \quad m-1 < \alpha \leq m, \quad m \in \mathbb{N}, \tag{32}$$

where

$$\left(\mathcal{I}_+^\alpha f\right)(z) \triangleq \left(\chi_+^{\alpha-1} * f\right)(z), \quad \alpha > 0 \tag{33}$$

is the causal α^{th}-order fractional integration of f. For specific conditions on f, refer to Zähle (1995). Similarly, the anti-causal fractional α^{th}-order derivative is defined according to

$$\left(\mathcal{D}_-^\alpha f\right)(z) \triangleq \left(\mathcal{D}^m \mathcal{I}_-^{m-\alpha} f\right)(z), \quad m-1 < \alpha \leq m, \quad m \in \mathbb{N} \tag{34}$$

with

$$\left(\mathcal{I}_-^\alpha f\right)(z) \triangleq \left(\chi_-^{\alpha-1} * f\right)(z), \quad \alpha > 0. \tag{35}$$

For simplicity denote fractional differentiation as $I^{-\alpha}$. Moreover,

$$\left(\mathcal{D}_+^{\alpha_1} \mathcal{D}_+^{\alpha_2} f\right)(z) = \left(\mathcal{D}_+^{\alpha_1+\alpha_2} f\right)(z) \tag{36}$$

$$\left(\mathcal{D}_-^{\alpha_1} \mathcal{D}_-^{\alpha_2} f\right)(z) = \left(\mathcal{D}_-^{\alpha_1+\alpha_2} f\right)(z). \tag{37}$$

Unlike for integer exponents, the operations of fractional integro-differentiation generally do not commute. See Gorenflo (1997) and references (to the Law of Exponents) therein.

Using the Fourier transform, fractional differentiation can be defined as

$$\left(\mathcal{D}_\pm^\alpha f\right)(z) = \mathcal{F}^{-1}\{(\pm j\zeta)^\alpha \hat{f}\}(z) \tag{38}$$

with $(\pm j\zeta)^\alpha \triangleq |\zeta|^\alpha \exp(j \operatorname{sign}(\pm\zeta)\frac{\alpha}{2}\pi)$.

Finally, notice that by generalizing differentiation to fractional differentiation, the operator kernels no longer decay fast and depend on direction.

[1] A wavelet is no longer a wavelet when the admissibility condition no longer holds, i.e. $\int \psi \neq 0$.

[2] Without proof it is assumed that this result also holds for fractional order moments.

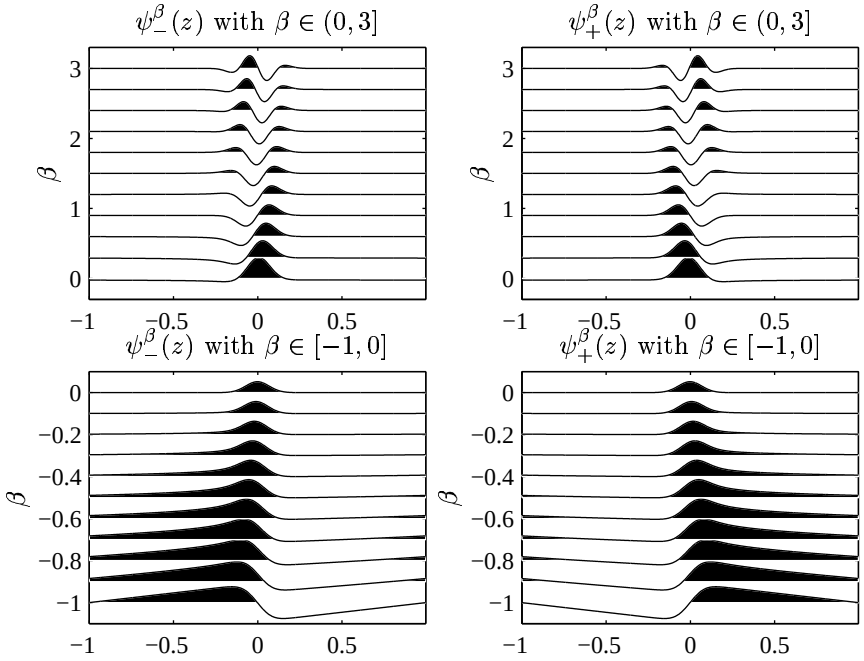

Figure 2: Generalized "wavelets". The wavelets are generated in the Fourier domain, which explains their periodicity. Top row (left): anti-causal, $\psi_-^\beta(z)$, and causal (right) wavelets $\psi_-^\beta(z)$ for $\beta \in (0,3]$. Bottom row (left): anti-causal, $\psi_-^\beta(z)$, and causal (right) "wavelets" $\psi_-^\beta(z)$ for $\beta \in [-1,0]$.

4.2 The β-transform

Given the definition for fractional differentiation, we are ready to generalize the definition of the CWT to a transform defined by multiscale causal/anti-causal differentiations,

$$\mathcal{W}\{f,\psi_\pm^\beta\}(\sigma,z) \triangleq \sigma^\beta \mathcal{D}_\pm^\beta \left(f * \phi_\sigma\right)(z) = \left(f * \psi_{\pm/\sigma}^\beta\right)(z) \quad \text{with} \quad \beta \in \mathbb{R}^+ \tag{39}$$

and $\psi_{\pm/\sigma}^\beta(z) = \sigma^\beta \mathcal{D}_\pm^\beta \phi_\sigma(z)$. The smoothing function is taken to be the Gaussian yielding,

$$\mathcal{W}\{f,\psi_\pm^\beta\}(\sigma,z) = \mathcal{F}^{-1}\{\left[(\pm j\sigma\zeta)^\beta e^{-(\sigma\zeta)^2}\right]\hat{f}(\zeta)\}(z), \tag{40}$$

where the action of the fractional-order wavelet is contained within the square brackets. Fig. 2 contains examples of causal and anti-causal $\psi_\pm^\beta(z)$'s with $\beta \in (0,3]$ (top row) and $\beta \in [-1,0)$ (bottom row). For the first β-interval the $\psi_\pm^\beta(z)$'s are still wavelets, but for the second (bottom row) the $\psi_\pm^\beta(z)$'s can no longer be considered as wavelets since $\int \psi_\pm^\beta(z) \neq 0$. The "wavelets" are computed by inverse Fourier transforming the expression between the brackets in Eq. 40, which explains their periodicity. Finally, as $\sigma \to 0$ $\mathcal{W}\{f,\psi_\pm^\beta\}(\sigma,z) \to (\mathcal{D}_\pm^\beta f)(z)$ for $f \in C^\alpha$ with $\beta > \alpha$.

Following Holschneider (1995), the conventional CWT of an algebraic onset function can be written as

$$\mathcal{W}\{\chi_\pm^\alpha,\psi\}(\sigma,z) \backsimeq \sigma^\alpha U_\pm^\alpha(\frac{z}{\sigma}) \tag{41}$$

with

$$U_\pm^\alpha(\frac{z}{\sigma}) = \mathcal{M}\{\psi(\mp\cdot\pm\frac{z}{\sigma})\}(\alpha+1). \tag{42}$$

The Mellin transform is given by

$$\mathcal{M}\{f\}(q) = \int_0^\infty \frac{\mathrm{d}t}{t} t^q f(t), \tag{43}$$

which is defined for a causal f (defined for $z \geq 0$) if

$$|f(z)| \leq c_1 z^{\alpha_1} \quad \text{for} \quad 0 < z \leq 1, \tag{44}$$

$$|f(z)| \leq c_2 z^{-\alpha_2} \quad \text{for} \quad 1 < z < \infty, \tag{45}$$

for some $c_1, c_2 > 0$, and $\alpha_1 < \alpha_2$. In this case the transform is analytic in the strip $\{z \in C : \quad \alpha_1 \leq \Re q \leq \alpha_2\}$. In case f is itself an onset function, i.e. $f(z) = \chi_{\pm}^{\alpha}(z)$, the region of convergence for Eq. 43 reduces to an empty strip (Kaiser, 1996), for which the Mellin transform still exists as a generalized function.

The number of vanishing moments, $M \in \mathbb{N}$, of the CWT are chosen such that $M \geq \lceil \alpha \rceil$, implying the order $\alpha \geq 0$ singularities to lie in the singularity observation window of the wavelet transform. The window is bounded from below (for negative α) by the wavelet's smoothness and from above by the number of vanishing moments. By generalizing the CWT to a transform with fractional order wavelets, $\psi \mapsto \psi_{\pm}^{\beta}$, the region of convergence is shifted, $\Re q = \alpha \mapsto \alpha + \beta$, implying

$$\mathcal{W}\{\chi_{\pm}^{\alpha}, \psi_{\pm}^{\beta}\}(\sigma, z) = \sigma^{\alpha} U_{\pm}^{\alpha+\beta}(\frac{z}{\sigma}). \tag{46}$$

This equation holds when $\psi_{\pm}^{\beta} \in C^{\infty}$, $\beta > \alpha$, such that $z_{\pm}^{\alpha}\psi_{\pm}^{\beta} \in L^1$. For $\beta \leq \alpha$ Eq. 43 no longer converges. In the Fourier domain this behavior corresponds to a divergence around the origin, which occurs when $(j\zeta)^{\beta-\alpha-1}$ exceeds $(j\zeta)^{-1}$. In that case the inverse Fourier transform is no longer locally integrable. By shifting towards fractional orders, a precise condition has been obtained for which the β-transform converges or diverges.

4.3 The βmml

As with the multiscale wavelet transform (Mallat and Hwang, 1992; Mallat, 1997), the β-transform modulus maxima (βMML) can be defined as follows:

Definition 4.1 (β-transform modulus maxima)
Let $\mathcal{W}\{f_{\pm}, \psi_{\pm}^{\beta}\}(\sigma, z)$ be the β-transform (cf. Eq. 39) of a causal/anti-causal function $f(z)$ defined for $\pm z \geq 0$ with $\beta > \alpha$.

- *A local extremum is any point (σ_0, z_0, β_0) for which $\partial_z \mathcal{W}\{f_{\pm}, {\psi_{\pm}}^{\beta_0}\}(\sigma_0, z)$ has a zero-crossing at $z = z_0$, when z varies.*
- *Call a β-transform modulus maximum, a βMM, any point (σ_0, z_0, β_0) such that $|\mathcal{W}\{f_{\pm}, \psi_{\pm}^{\beta_0}\}(\sigma_0, z)| < |\mathcal{W}\{f_{\pm}, \psi_{\pm}^{\beta_0}\}(\sigma_0, z_0)|$ when z belongs to either the right or the left neighborhood of z_0, $|\mathcal{W}\{f_{\pm}, \psi_{\pm}^{\beta_0}\}(\sigma_0, z)| \leq |\mathcal{W}\{f_{\pm}, \psi_{\pm}^{\beta_0}\}(\sigma_0, z_0)|$ when z belongs to the other side of the neighborhood of z_0.*
- *Call a β-transform modulus maxima line, a βMML, any connected curve in the β space (β, z), σ fixed, along which all points are modulus maxima.*

4.4 The on/off criteria

Similar to WTMML's, βMML's contain information on the local behavior of f, within a cone given by $z/\sigma =$ constant. In this paper, we are only interested in obtaining estimates for the unknown coarse-grained, local scale exponent α at a fixed scale. For this purpose it suffices to look at the onset of a βMML as a function of position and β within a fixed-scale of the zoom. With a slight abuse of notation, the following criterion provides the fixed scale estimate for $\alpha, \beta \geq 0$

$$\alpha(\sigma_0, z_0) = \inf_{\beta}\{\beta : \partial_z \mathcal{W}\{f_{\pm}, \psi_{\pm}^{\beta}\}(\sigma_0, z = z_0) = 0\}, \tag{47}$$

for a causal/anti-causal function $f_{\pm}(z)$ containing an (coarse-grained) algebraic singularity at $z = z_0$. This criterion is inspired by the work of Zähle (1995), and argues that under certain conditions on $f_{\pm}(z)$,

$$\left(\mathcal{D}_{\pm}^{\beta} f_{\pm}\right)(z) = \begin{cases} 0 & \text{for} \quad \beta < \alpha(z) \\ \infty & \text{for} \quad \beta > \alpha(z), \end{cases} \tag{48}$$

which in the coarse-grained case corresponds to the emergence of a local maximum. By taking $\sigma \to 0$ in Eq. 47, the criterion becomes equivalent to Eq. 48. But notice the necessary distinction in direction. For $\alpha < 0$ a similar criterion can be derived by reversing the argument, stating

$$\alpha(\sigma_0, z_0) = \sup_{\beta}\{\beta : \partial_z \mathcal{W}\{f_{\pm}, \psi_{\pm}^{\beta}\}(\sigma_0, z = z_0) = 0\} \tag{49}$$

with $\alpha, \beta < 0$. Here, the β-transform as defined in Eq. 39 is extended to include β-order fractional integrations.

The first criterion (cf. Eq. 47) is based on the property that when $\alpha > 0$, a local maximum appears if the order of fractional differentiation exceeds the order of the transition infinitesimally. Conversely, the second criterion (cf. Eq. 49) uses the property that a local maximum disappears when the fractional integration exceeds the negative scaling exponent. Differentiation, in the distributional sense, of onset functions $\alpha \geq 0$ reduces the exponent by the order of differentiation. For example, during reflection the deconvolved[3] reflectivity involves a single differentiation of the medium fluctuations, yielding negative α in case of medium fluctuations with $0 < \alpha < 1$.

At the point of onset/disappearance, the location of the singularity is not well-resolved. Depending on direction, the location tends to be biased towards the left or right. To circumvent this problem the βMML is followed until the order of differentiation exceeds the estimated exponent by at least 1.

Notice that both criteria of Eq.'s 47 and 49 are based mainly on heuristical arguments valid for singular functions of the type

$$\Delta f(z) \triangleq \sum_{n \in N} c_+^n \chi_+^{\alpha_n}(z - z_n) + c_-^n \chi_-^{\alpha_n}(z - z_n), \tag{50}$$

with $(c_+^n \neq 0 \wedge c_-^n = 0) \vee (c_+^n = 0 \wedge c_-^n \neq 0)$ and $c_+^n c_-^{n+1} > 0$ the magnitudes such that $\Delta f(z_n - \epsilon) = \Delta f(z_n)$, and z_n's the abscissa. Singularities in these singular functions can, for scales exceeding the inter-singularity distance, no longer be treated as isolated. This implies that the smoothing function should be of compact support. By limiting the number of modulus maxima per cone of influence to one, we are partially able to eliminate the effects of the non-vanishing support for the Gaussian.

The method we propose can now be formulated as follows:

Procedure 4.1 (Monoscale measurement and detection of singularities)

1. ***Select*** *wavelets with decreasing β such that $\beta_0 < \alpha < \beta_1$.*
2. ***Fix*** *σ such that possible high frequency noise is reduced.*
3. ***Compute*** *the generalized wavelet transform with Eq. 39 for $\beta \in [\beta_0, \beta_1]$.*
4. ***Locate*** *βMM's with definition 4.1, working from large to small β's.*
5. ***Create*** *the set $\beta_\pm = \{1, 2, \ldots, l\}$ of l curves, parameterized by $\{Z(\sigma, \beta)\}_{m \in \beta_\pm}$.*
6. ***Check*** *$\{Z(\sigma, \beta)\}_{m \in \beta_\pm}$'s lie inside the cone of influence ($|z - z_m| \leq K\sigma$).*
7. ***Apply*** *Eq.'s 47-49, yielding $\alpha_m = \alpha(z_m)$ as the $\inf_\beta$ along the m^{th} βMML.*
8. ***Remove*** *from α_m those estimates for which α_m lies too close to $[\alpha]$ or $\inf\ \beta$.*
9. ***Keep*** *α_m for which one of the two criteria holds for* ***both*** *directions.*
10. ***Determine*** *z_m by following the βMML until $\beta = \alpha_m + 1$ or $\sup \beta$.*
11. ***Determine*** *$c_\pm^m = \mathcal{W}\{f, \psi_\pm^{\gamma_m}\}(\sigma, z_m)$ with $\gamma_m = \alpha_m + 1$ or $\sup \beta$.*
12. ***Determine*** *the direction for each singularity.*
13. ***Remove*** *those $c_\pm^m c_\pm^{m+1} < 0$ with $\pm_m = + \wedge \pm_{m+1} = -$.*

Items 8, 9 and 13 are necessary to eliminate βMM's caused by either causal/anti-causal singularities, analyzed by the wrong anti-causal/causal analyzing wavelets, or by cusp-like singularities. In the first case, the generalized wavelet transform gives rise to an extra erroneous extremum. This extremum is an artifact caused by a response which, in case of an opposite direction wavelet, is given by the Hilbert transform. Extrema caused by cusp-like singularities can be removed by extending the search to left and right neighborhoods with an asymmetric cone. Locations and magnitudes are obtained at values for β such that the singularity becomes locally delta-like, which corresponds to a local pre-whitening. Finally, we note that the items in the above procedure are for a large part based on heuristics and require further justification and proof. For example, it remains an open problem how to deal with the directional problem of cusp-like singularities (not strictly (anti)-causal).

[3] Under the assumption that deconvolution removes a possible additional differentiation by the seismic wavelet, e.g. the twofold differentiation of a Ricker wavelet.

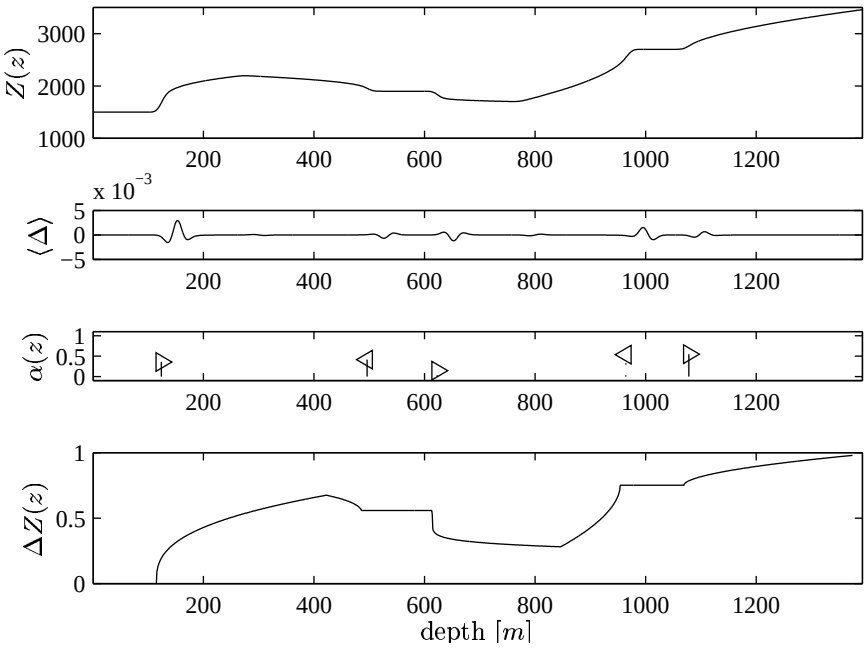

Figure 3: Directional local regularity analysis and reconstruction of a synthetic post-stack migrated reflectivity trace (obtained by the stacking procedure illustrated in Fig. 1). Post-stack reflectivity for a Ricker wavelet corresponds to the smoothed third derivative of the acoustic impedance function. For reference the smoothed impedance profile is plotted in the first plot. Second plot: imaged reflectivity; Third plot: source wavelet corrected ($\alpha \mapsto \alpha + 3$) local regularity, directivity and sign estimates. Solid $\triangleright$'s are causal positive, $\triangleleft$ anti-causal positive, dotted $\triangleright$ causal negative sign, dotted $\triangleleft$ anti-causal negative sign. Bottom plot: reconstructed acoustic impedance profile.

4.5 Reconstruction

Reconstruction of functions with fluctuations, defined by Eq. 50, is possible given estimates for the location, direction, regularity and relative magnitude for the observed singularities. For instance (see e.g. Example 4.1), the fluctuations can be reconstructed from estimates obtained from the smoothed first derivative (read reflectivity) of the original function. We base the reconstruction procedure on Eq. 50 with the parameters set by the estimated values, supplemented with additional conditions. The reconstruction procedure can be defined as follows:

Procedure 4.2 (Reconstruction)

1. **Normalize** the magnitudes, $c_{\pm}^{m}$ such that $\sum_{m\in\beta_{\pm}} c_{\pm}^{m} = 1$.
2. **α-correction** (optional), $\alpha_m \mapsto \alpha_m + \alpha_{\text{cor}}$.
3. **For** each $m \in \beta_{\pm}$ take the estimated z_m, $\pm_m$, α_m, $c_{\pm}^{m}$.

   if $(\pm_m = \pm_{m+1})$ then

$$f(z) = \chi_{\pm_m}^{\alpha_m}(z - z_m)1_{[z_m, z_{m+1})} \tag{51}$$

   else

$$f(z) = \chi_{\pm_{m+1}}^{\alpha_m}(z - z_{m+1})1_{(z_m, z_{m+1}]}. \tag{52}$$

   if $(\pm_m \neq \pm_{m+1}) \wedge (\pm_m = +)$ then

$$f(z) = \inf\{\chi_{+}^{\alpha_m}(z - z_m)1_{[z_m, z_{m+1})}, \chi_{-}^{\alpha_{m+1}}(z - z_{m+1})1_{(z_m, z_{m+1}]}\} \tag{53}$$

for $c_+^m, c_-^{m+1} > 0$ and

$$f(z) = \sup\{\chi_+^{\alpha_m}(z - z_m)1_{[z_m, z_{m+1})}, \chi_-^{\alpha_{m+1}}(z - z_{m+1})1_{(z_m, z_{m+1}]}\} \tag{54}$$

for $c_+^m, c_-^{m+1} < 0$.

4. **Smoothing** (optional), $f(z) \mapsto (f * \phi_\sigma)(z)$.

Reconstructions using procedure 4.2 are *modulo* polynomials, which is consistent with the behavior of the inverse wavelet transform. The optional α-correction takes care of a possible additional differentiation, which would be ($\alpha_{\text{cor}} = 1$) when reconstructing the medium from the imaged, deconvolved reflectivity. For cases where causal singularities are followed by anti-causal ones, reconstruction creates an additional singularity at the location where the two reconstructions meet. Generally, this singularity will not be important because of its relatively large regularity.

Example 4.1 (Synthetic example)
Fig. 3 demonstrates the application of the monoscale analysis and reconstruction to a single post-stack imaged reflection trace (see Fig. 1 (bottom left)). The medium consists of 5 *transitions with* $\pm \in \{1, -1, 1, -1, 1\}$ *and* $\alpha \in \{0.25, 0.39, 0.15, 0.52, 0.60\}$. *For a Ricker wavelet, the stacked reflectivity (Fig. 3 (second row)) corresponds to the smoothed derivative of the acoustic impedance which is displayed in Fig. 3 (top). Singularity estimates, after correction for the differentiation, are plotted in the third row of Fig. 3. Solid* $\triangleright$*'s symbols are used for causal positive sign reflectors,* $\triangleleft$ *for anti-causal positive reflectors, dotted* $\triangleright$ *for causal negative sign reflectors, and dotted* $\triangleleft$ *for anti-causal negative signs. Clearly, the method finds and characterizes the singularities accurately. Given the location, direction and order of the singularities, a pseudo-acoustic impedance profile is generated using the reconstruction, as described in procedure 4.2. The magnitude of the reflectivity at the location of the singularities is used to define the relative magnitudes of the transitions (the* $c_\pm^m$*'s). Fig. 3 (bottom) displays the reconstructed profile. As expected, the method is not able to retrieve the actual impedances. Instead, the reconstruction recovers the singularities in the fluctuations. Deviations occur when causal singularities are followed by non-causal ones. In that case the method lacks information on where to connect the two functions (e.g. between the first and second transitions). Finally, notice that the reconstruction is not smoothed which, under the assumption that coarse-grained singularities persist to finer scales, corresponds to an effective deconvolution (together with the exponent correction for the differentiation by the Ricker).*

4.6 Application to seismology

During the seismic imaging process, amplitudes remain difficult to control. Consequently, full inversion toward the earth's medium properties has not always been successful. We know that the composition of the forward and inverse map $(\mathbf{L}^* \circ \mathbf{L})(z)$ is approximately pseudo-differential, and as a result, we can be confident that major singularities are likely to be preserved during the seismic imaging process. For the purpose of geological horizon delineation, interpretation and reconstruction, it suffices to characterize singularities by finding their location and measuring their order.

4.6.1 Well Data

Fig. 4 demonstrates the application of our method to a real earth acoustic impedance profile obtained from a well-log measurement. The sampled (sample rate is 1 m) data were analyzed using procedure 4.1. Fig. 4 contains both the monoscale analysis for $\beta \in [-0.75, 3]$ and the reconstruction of a pseudo well from a coarse-grained singularity map. This coarse-grained map is obtained by smoothing the fine-grained (see Fig. 4, second plot thin line) acoustic impedance profile with a ($\sigma = 6$) Gaussian kernel. The estimated regularity and magnitude estimates are depicted by gray-scale circles (Fig. 4, top). Positions of the gray-filled circles point to the location of the singularities. The gray-scales themselves refer to the order, and the size to the magnitudes of the derivative of the smoothed well *at* the locations of the singularities. The gray-scale bar on the right defines the orders corresponding to the different gray-values. Dark shades are used to delineate the sharp, i.e. irregular, transitions which in the Fourier domain tend to cause "blue divergences". The color white, on the other hand, indicates smooth transitions, which in the Fourier domain correspond to "infrared divergences". Clearly, one can see that the irregular gray-value changes support the observation that well data behave multifractally (Muller et al., 1992; Saucier and Muller, 1993; Herrmann, 1997, 1998b, 2000). Moreover, the emergence of circles almost everywhere

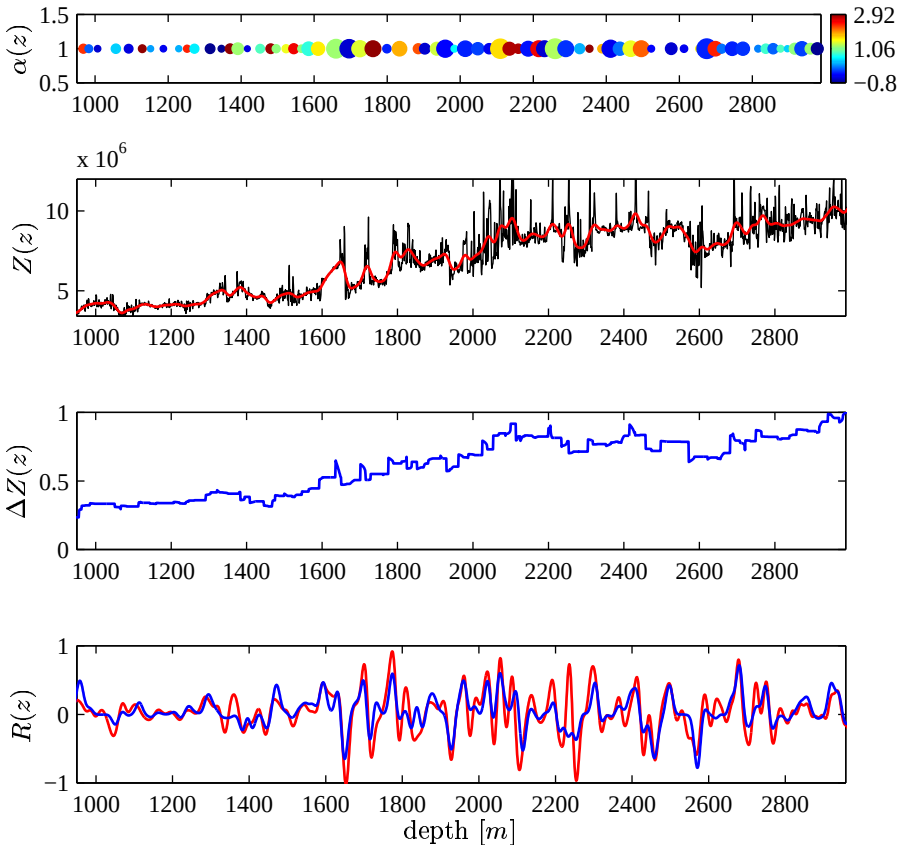

Figure 4: Application of the monoscale method to a smoothed Mobil well-data set Keys and Foster (1998). Top: singularity characterization with $\beta \in [-1, 3]$, the gray-scale bar defines singularity orders and the circle size the relative magnitude. Second plot: smoothed ($\sigma = 6$), thick line) and fine-grained (thin line) acoustic impedances. Third plot: reconstructed pseudo well, based on the singularity characterization, plotted in the first plot. The pseudo well contains different order reflectors and yields a reflectivity (solid line bottom plot) close to that of the smoothed original well (dashed line).

is an indication of an accumulation of singularities. The third plot contains the reconstructed profile using singularity characterization. Note the sharpness variations of the reconstructed transitions. At the bottom, comparison is made between the first derivative of the original smoothed acoustic impedance and the derivative (read reflectivity), obtained by smoothing and differentiating the reconstructed profile. Although the reconstruction is not perfect, the result is encouraging because the pseudo-reflectivity matches the reflectivity from the original quite well.

4.6.2 Seismic Images

The results of applying the monoscale analysis method to a post-stack, time-migrated section are summarized in Fig.'s 5 and 6. Simply speaking, time migration differs from depth migration by staying in time rather then converting to depth. Hence, the vertical axis of Fig. 5 corresponds to the two-way traveltime. The horizontal axis measures the lateral direction. Migration amplitudes are depicted in gray-scale and reveal part of the reflector structure in the earth subsurface.

By conducting the monoscale analysis on each individual vertical trace of the migrated data (Fig. 5, top), we create a map of the earth's singularity structure. This map is depicted in Fig. 5 (middle) and was generated using $\beta \in [-4, 1]$ and $\sigma = 1$, respectively. Gray-scales are used to display the singularity map by a scatter plot. The gray-scales of this scatter plot are related to the local regularity of the vertical variations in reflection amplitude. The dark shades refer to relatively sharp reflectors, while the white shades mark the relative smooth transitions. Notice the location and, to a lesser extent the gray-scale, to be captured in a laterally-consistent manner, even though the amplitudes show relative large variations along the major reflector horizons. Refer to Herrmann and Stark (2001); Lyons and Herrmann (2001) for a discussion on the geological interpretation of the singularity map. Finally, Fig. 5 (bottom) contains the reconstructed pseudo reflectivity. The reconstruction is based on the location and gray-scales of the singularity scatter plot (Fig. 5, middle) in conjunction with the relative magnitude of the reflectivity at the location of the singularities. Clearly, the reconstruction captures the major features of the original reflection data quite well, although there are trace to trace variations. Finally, notice that both the singularity map and the reconstruction display a nice consistency across the wells located at trace #'s 205 and 365. The wells are tied to the seismic data by forward modeling a synthetic reflectivity. This reflectivity is computed using Eq. 1, with the medium given by the well-log profile and the source wavelet estimated so as to minimize the difference between the synthetic and the imaged surrounding reflectivity. For clarity, the synthetic trace is repeatedly plotted.

Finally, Fig. 6 illustrates more details of the monoscale analysis and reconstruction. For this purpose the area surrounding the second well (white box in Fig. 5, top) is examined. Fig. 6 (top) displays both the synthetic reflection amplitudes (middle) and real earth imaged reflectivity (sides). Besides the wiggle traces, this plot also contains the *locii*, order and relative magnitudes of the singularities. Again, the position of the circles refers to the location of the singularities, while the gray-scale and size refer to the singularity strength and relative magnitude. As one can see there is a reasonable lateral consistency for the gray-scale along the major reflection horizons, persisting across the synthetic traces (around trace # 15). As an ultimate test, reconstruction results for both the pseudo reflectivity and well are depicted in the bottom two plots of Fig. 6. These results are compared to data we actually know from the well-log. What these results clearly demonstrate is that the proposed singularity inversion method works quite well, despite the severe bandwidth limitation of the seismic data (middle), compared to the well (bottom). The reconstructed impedance (solid line) follows the original well for most of the major transitions. The estimated transitions vary in regularity/sharpness, but are limited in number because of the limited resolution of the seismic data. Still, the transitions capture the leading order scaling behavior of the transitions at the seismic length scale.

5 Scale analysis by Fractional Spline Matching Pursuit

Results of the previous section have shown that information on the singularities can be obtained from bandwidth limited seismic data. As we will show below (in section 6) the *modulus maxima* method excels in finding the location of the singularities. However, the method has difficulties with estimating the transition's direction (causal *versus* anticausal). This difficulty may not only limit our interpretation but also makes the reconstruction less accurate. Moreover, the infinite extent of the generalized transitions prevent reconstruction (see Procedure 4.2).

Unser and Blu (2000) propose an approach based on a generalization of splines to fractional splines, defined by algebraic onset functions as were introduced in Section 4. These onset functions entail a

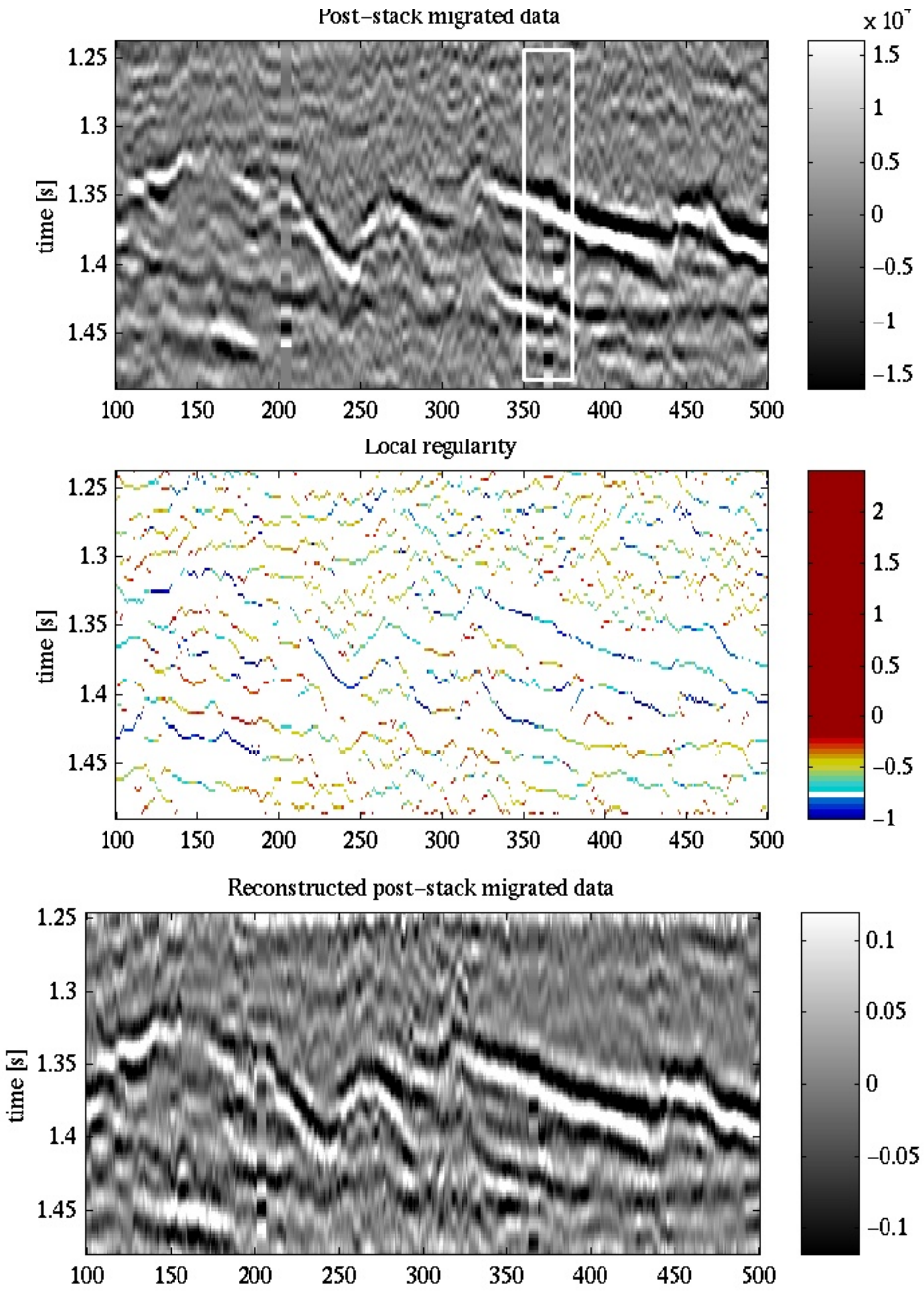

Figure 5: Time migrated Troll dataset and its reconstruction, using the singularity characterization with $\beta \in [-4, 1]$ and $\sigma = 1$. Top: in gray-scale the imaged reflection amplitudes. Middle: scatter plot of the estimated singularities; gray-values of the dots refer to the corrected singularity orders (darker means more irregular/sharper). Bottom: trace by trace reconstruction of the reflectivity, based on the location, order and relative seismic amplitude. Both the position and order of the reflectors are well recovered. The correction for the singularity order was $\alpha_{\text{cor}} = 3$. The singularity structure aligns nicely with the imaged reflectors. Good lateral consistency is obtained along the major reflectors and across the wells located at trace #'s 205 and 365. These wells are tied to the seismic by generating synthetic reflectivity using Eq. 1 and a source wavelet estimate. The trace by trace basis of the method is responsible for the apparent horizontal differences in the reconstruction.

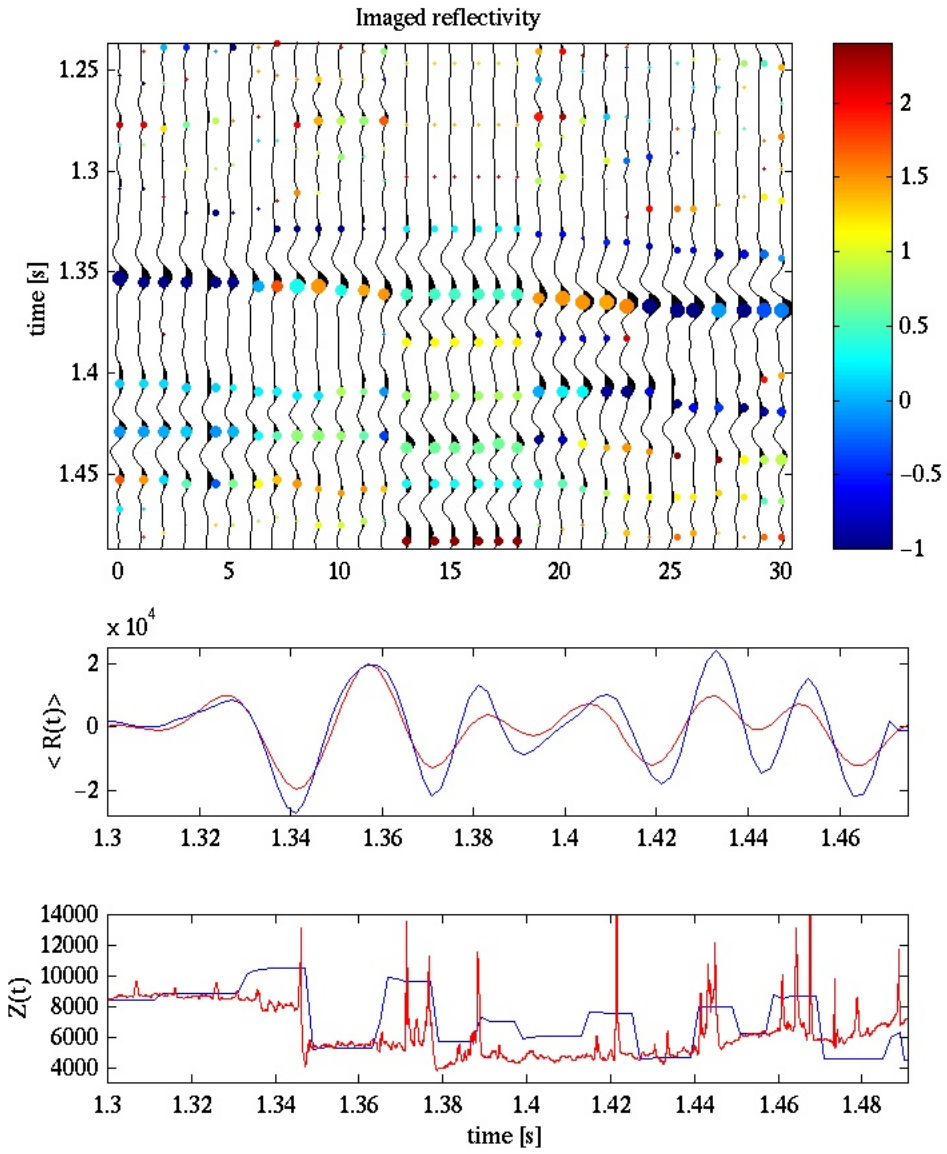

Figure 6: Details of reflectivity and pseudo well-log reconstruction, based on singularity characterization. Top: wiggle plot of the selected migration amplitudes (within the white box in Fig 5, top) together with the estimated singularity orders, depicted by the gray-colored circles whose size depend on the relative amplitudes. Middle: seismic reflectivity (dashed) at the well (around trace # 15 in top plot) and the reconstructed reflectivity (solid). Bottom: reconstructed well (solid) and the original well (dashed). Notice, the remarkable reconstruction despite the severe bandwidth limitation of the seismic (compare reflectivity to the detailed well).

generalization of the knots in spline decompositions, which are normally given by jump discontinuities. In this section the successive steps underlying our greedy atomic decompositon algorithm will be reviewed, resulting in the definition of a Fractional Spline Wavelet Packet Matching Pursuit Algorithm. First, we re-introduce generalized transition models (in the same spirit as in section 4), followed by a discussion on Fractional Splines, Fractional Spline Wavelets, Wavelet Packet Basis and the Matching Pursuit search algorithms. This latter algorithm underlies our non-linear and greedy atomic decomposition of the data.

5.1 Generalized onsets

As stated earlier multifractal scaling data (e.g. media) can be thought to consist of accumulations of varying order transitions/singularities of the type:

$$\chi_{\pm}^{\alpha}(z) \triangleq \begin{cases} 0 & z \leq / \geq 0 \\ \frac{z^{\alpha}}{\Gamma(\alpha+1)} & z > / < 0. \end{cases} \tag{55}$$

These depth-z and index-α onset functions (Herrmann, 1997; Herrmann and Stark, 2000; Herrmann, 2001) define the causal $\chi_{+}^{\alpha}(z)$, anti-causal $\chi_{-}^{\alpha}(z)$ and symmetric cusp-like $\chi_{*}^{\alpha}(z) = \chi_{+}^{\alpha}(z) + \chi_{-}^{\alpha}(z)$ transition models. Compared to the method described in Section 4, symmetric cusp-like transitions are also allowed, under the condition that $c_{+} = c_{-}$ (cf. Eq. 28). As we will show later (cf. Section 6), these onsets form the basis of our facies characterization (Harms and Tackenberg, 1972; Emery and Meyers, 1996) referring to (1) *coarsening* upward sequences; (2) *fining* upward sequences and (3) *symmetric* lobe shape sequences. In the first two cases, the transition is marked by a single onset, whose sharpness and scaling properties are characterized by the order parameter α, while lobe-shaped onsets are marked by sharp onsets from both top and bottom. For $\alpha = 0$, the onset becomes a jump discontinuity and for $\alpha = 1$ a ramp function. Sharpness α is characterized irrespective of the scale, and determines the *order of magnitude* of the variations at the onsets. For notational consistency with the Fractional Spline literature, we use α for both the transition order and the Fractional Spline order. Refer to Section 6 for a detailed discussion on facies for lithological boundaries. Fig. 20 illustrates the significance of sharpness for both the transition shape and reflection signature.

5.2 From Splines to Fractional Splines

Conventional degree-m splines are piecewise m^{th}-order polynomials smoothly joined together at knots. At these knots the m^{th}-order derivative contains a jump discontinuity. For uniform unit spacing of the knots, splines can uniquely be characterized by a summation of B-splines,

$$f(z) = \sum_{k \in \mathbb{Z}} a_k \beta^m (z - z_i), \tag{56}$$

where the splines are given by m^{th}-order auto-convolutions of the boxcar function, i.e.

$$\beta^m(z) \triangleq (\underbrace{\beta^0 * \beta^0 * \cdots * \beta^0}_{(m+1) \quad \text{times}})(z) \tag{57}$$

with $\beta^0(z)$ being the indicator function on $z \in (-\frac{1}{2}, +\frac{1}{2})$. In the Fourier domain this definition for the B-splines corresponds to raising the sinc-function to the $(m+1)^{th}$-power. Following Unser and Blu (2000); Blu and Unser (2000), we can generalize integer order splines to fractional α-order splines by raising the sinc-function to fractional powers. In the space domain this generalization corresponds to the $\alpha + 1$-order fractional difference of the onset function defined in Eq. 55,

$$\beta_{\pm}^{\alpha}(z) \triangleq (\Delta_{\pm}^{\alpha+1} \chi_{\pm}^{\alpha})(z), \quad \beta_{*}^{\alpha}(z) \triangleq (\beta_{+}^{\frac{\alpha-1}{2}} * \beta_{-}^{\frac{\alpha-1}{2}})(z) \tag{58}$$

where

$$(\Delta_{\pm}^{\alpha} f)(z) \triangleq \sum_{k \geq 0} (-1)^k \binom{\alpha}{k} f(z \mp k). \tag{59}$$

In Eq. 58 β_{+}^{α}, β_{-}^{α} and β_{*}^{α} refer to the causal, anticausal and symmetric Fractional Splines, respectively. Likewise, generalized onsets direction distinctions are being made.

5.3 Properties Fractional Splines

As shown by Unser and Blu (2000), Fractional Splines are in Ł^2 because $\hat{\beta}(\omega)$ is bounded and $\hat{\beta}(\omega) \sim \omega^{-\alpha-1}$ as $\omega \to \infty$. To be more precise

$$\beta^{\alpha}_{+,*} \in W_2^r \quad \text{with} \quad r < \alpha + \frac{1}{2}, \tag{60}$$

where W_2^r is the index-r Sobolev space ($f \in W_2^r$ if $f \in$ Ł$^2 \quad \wedge \quad \partial^r f \in$ Ł^2). In addition, Fractional Splines can be seen as functions that are Hölder regular-α at the knots, which, from now on, are assumed to be located at the integers. Finally, Fractional Splines adhere to the following two-scale relation

$$\beta^{\alpha}(\frac{z}{2}) = \sum_{k \in \mathbb{Z}} h^{\alpha}(k) \beta^{\alpha}(z-k), \tag{61}$$

where the refinement filter is given by

$$\hat{h}^{\alpha}_{+}(\omega) = 2\left(\frac{1+e^{-j\omega}}{2}\right)^{\alpha+1}, \quad \hat{h}^{\alpha}_{*}(\omega) = 2\left|\frac{1+e^{-j\omega}}{2}\right|^{\alpha+1} \tag{62}$$

and $h^{\alpha}_{-}(\cdot) = h^{\alpha}_{+}(-\cdot)$. Refer to Unser and Blu (2000) for a more detailed discussion on Fractional Splines.

5.4 Fractional Spline Wavelets

As with ordinary spline wavelets, Fractional Spline Wavelet bases can be formed via an orthogonalization process (Unser and Blu, 2000), yielding an expression for the refinement filter. Following Unser and Blu (2000) this filter can be found by computing the inverse of the square root of the fractional B-spline auto-correlation function

$$a_{\varphi}(k) \triangleq \langle \beta^{\alpha}(\cdot), \beta^{\alpha}(\cdot - k) \rangle = \beta^{2\alpha+1}_{*}(k), \tag{63}$$

yielding the following expression for for the orthogonal smoothing function

$$\phi^{\alpha}(z) = \sum_{k \in \mathbb{Z}} (a^{\alpha}_{\varphi}(k))^{-1} \beta^{\alpha}(z-k). \tag{64}$$

References to subscripts of β are ommited when the expressions are valid for all directions. The corresponding two-scale relationship reads

$$\phi^{\alpha}(\frac{z}{2}) = \sqrt{2} \sum_{k \in \mathbb{Z}} h_0(k) \phi^{\alpha}(z-k). \tag{65}$$

with the refinement filter

$$\hat{h}_0(\omega) = \sqrt{\frac{\hat{a}_{\varphi}(\omega)}{\hat{a}_{\varphi}(2\omega)}} \sqrt{2} \left|\frac{1+e^{-j\omega}}{2}\right|. \tag{66}$$

Given this filter we can now write the two-scale relation for Fractional Wavelets as follows:

$$\psi^{\alpha}(\frac{z}{2}) \triangleq \sqrt{2} \sum_{k \in Z} g_0(k) \psi^{\alpha}(z-k) \tag{67}$$

with g_0 computed using Mallat's recipe $\hat{g}_0(e^{\omega}) = e^{j\omega} \hat{h}_0(-e^{-j\omega})$. See Blu and Unser (2000) for detail, software available at `http://bigwww.epfl.ch/blu/fractsplinewavelets/index.html`. For examples of Fractional Splines see Fig. 7-(top).

5.5 Properties Fractional Spline Wavelets

Generalizing spline wavelets (also known as Battle-Lemarié wavelets) to their fractional counterpart has several advantages. First of all the wavelets and smoothing function's regularity are directly related to the order α, ϕ^{α}, $\psi^{\alpha} \in C^{\alpha}$. Furthermore the wavelets vanishing moments are given by the entier (smallest integer exceeding α, i.e. $\lceil \alpha \rceil$) while their linear approximation error also becomes fractional, i.e. $\alpha + 1$.

Compared to ordinary m^{th}-order spline wavelets, α-order spline wavelets act as smoothed fractional $(\alpha+1)^{\text{th}}$-derivative operators, i.e. for low frequencies $\hat{\psi}^{\alpha}_{\pm}(k) \sim (\pm jk)^{\alpha+1}$ and $\hat{\psi}^{\alpha}_{*}(k) \sim k^{\alpha+1}$. This

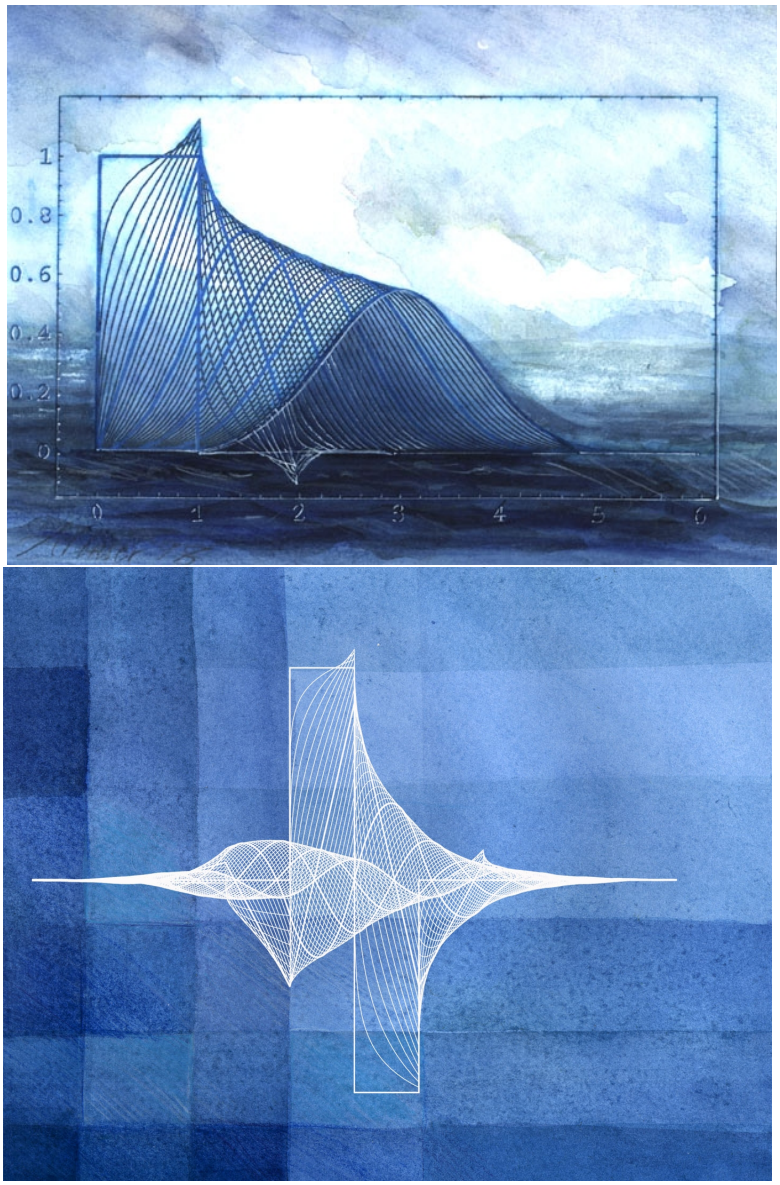

Figure 7: Artistic examples of Fractional Splines (by Annette Unser courtesy Michael Unser) (top) and causal Fractional Spline Wavelets (bottom) for $\alpha \in (-0.5, 2]$. Note the symmetry for integer odd α's.

means that Fractional Spline Wavelets can not only be used as approximate whiteners within decon. and kriging (see Kane and Herrmann in this report) but can also be used as "smoothness-" adapted atoms in a Wavelet Packet Dictionary (Coifman et al., 1992). This choise is very appropiate since seismic reflectivity itself behaves as a smoothed fractional derivative for transitions of the type given in Eq. 55 (with $\alpha < -1$ after, say, subtracting $2+1$, where 1 refers to the differentiation defining the reflectivity and the 2 refers to differentiations of the Ricker wavelet). Finally, as $\alpha \to \infty$, we can show that fractional spline wavelets converge to modulated Gaussians, which define the optimally time-frequency localized Gabor atoms (Mallat, 1997). Examples of Fractional Spline Wavelets for increasing α are depicted in Fig. 7-(bottom).

5.6 Fractional Spline Wavelet Packet Bases

Fractional Spline Wavelet Bases $\{\psi^{\alpha}_{\pm,*}(z) = \frac{1}{2^j}\psi^{\alpha}_{\pm,*}(\frac{z-2^j n}{2^j})\}_{(j,n)\in Z^2}$ form an orthogonal basis, which can be used to decompose and approximate f in $\mathcal{O}(N)$ operations for signals of size N (Mallat, 1997). These decompositions are not necessarily adapted to particular properties of f. Wavelet Packet Bases, on the other hand, provide a redundant (frame) signal-adaptive decomposition of the signal f into Wavelet Packed Bases in $\mathcal{O}(N \log N)$ operations. In case of the Wavelet Packets, the frequency axis is divided into separate various size intervals (in case of Local Cosine Basis, the time axis would be subdivided into various length intervals). Contrary to the ordinary wavelet transform, both the scaling and wavelet functions are applied to data, generating a full dyadic tree of details and smoothings (See e.g. Mallat (1997) for detail). From this redundant tree, one could either try to select a best basis and/or select the mostly "coding" individual atoms with a sub-optimal greedy search algorithm, based on a correlation measure between the data's "events" and atoms. With this algorithm we will be able to (1) select only a limited number of vectors to represent the signal; and (2) "improve" the decomposition by order and direction adaptation of the elements in the Wavelet Packet Bases. We used " " to indicate that, for $f \in W^r$ with $r > 0$ regularity adaptation will not improve the asymptotic convergence rate (as long as the number of vanishing moments of the wavelet exceeds r) of the non-linear selection mechanism. However, the adaptation may certainly improve the "constant" in the asymptotics while for negative Sobolev/Besov spaces ($r < 0$), there are, to our knowledge, no convergence results. Moreover, we hope to use the additional parametrization of the atoms – by the continuously varying α and 3 different directions – as a more precise characterization for the scaling (by α) and phase (by α and direction) characteristics of the coarse-grained singularities. Since the size of the dictionary increases by a factor $C = 3 \times \#\alpha$, the non-linear sub-optimal Matching Pursuit Search Algorithm (Mallat, 1997) seems to be an obvious choice.

5.7 Atomic decomposition by Matching Pursuit

Following Mallat (1997), we use a greedy algorithm for the decomposition of f from the redundant dictionary. The algorithm is based on minimizations of the L^2-norm difference between reductions of f and the atoms g_γ with $\gamma \in \Gamma$. Reductions are projections of f:

$$f = \langle f, g_{\gamma_0}\rangle g_{\gamma_0} + Rf, \tag{68}$$

where Rf is the residue and g_{γ_0} a particular γ_0-indexed atom (Mallat, 1997). The dictionary we use is formed by multiple directional Fractional Spline Wavelet Packet Bases, i.e. $\mathcal{D} = \{g_\gamma\}_{\gamma\in\Gamma}$ with g_γ defined by wavelet packets generated by the α^{th}-order (anti)-causal/symmetric Fractional Spline Wavelets (as defined in Eq. 67). The index γ refers to the location in the tree (scale and sample number), direction and order.

Repeating the above procedure yields the following atomic decomposition algorithm:

Procedure 5.1 (Matching Pursuit (Mallat, 1997))

1. Initialize: *Set* $m = 0$ *and compute* $\{g_\gamma\}_{\gamma\in\Gamma}$.
2. Best match: *Find* $g_\gamma \in \mathcal{D}$ *such that*

$$|\langle R^m f, g_{\gamma_m}\rangle| \geq \nu \sup_{\gamma\in\Gamma} |\langle R^m f, g_\gamma\rangle|. \tag{69}$$

3. Update: *For all* $g_\gamma \in \mathcal{D}$ *with* $\langle g_{\gamma_m}, g_\gamma\rangle \neq 0$

$$\langle R^{m+1} f, g_\gamma\rangle = \langle R^m f, g_\gamma\rangle - \langle R^m f, g_{\gamma_m}\rangle\langle g_{\gamma_m}, g_\gamma\rangle. \tag{70}$$

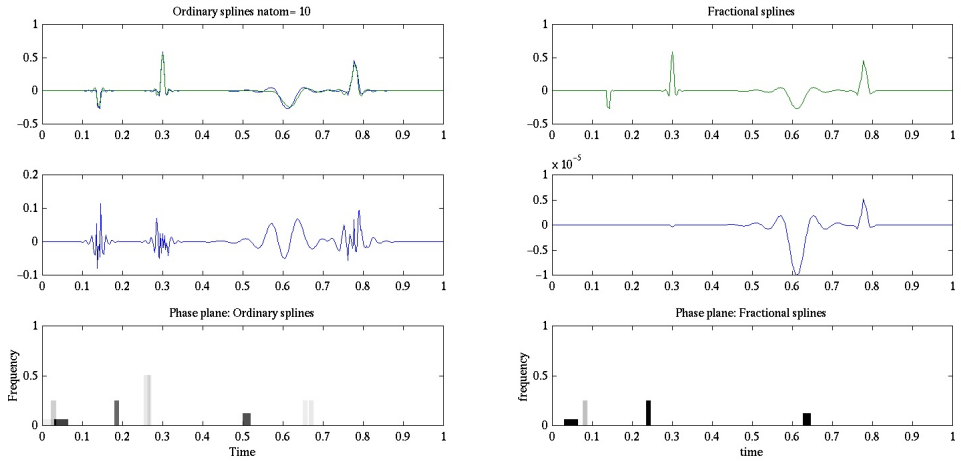

Figure 8: Atomic (de)-composition of a synthetic trace by (right) $M = 3$ and fractional $\alpha \in [0.1, 3.5]$ $+$, $-$, $*$ splines (left). Top: original (blue) and reconstructed (green). The original was generated with Eq. 72 and scale, $\sigma = 2^j$ with $j = 2, 2, 4, 3$, $\alpha = 0.1, 1.2, 3.5, 0.7$ and directions $+, +, -, -$. Middle: error. Bottom: time-frequence plane.

4. Stop: *If*

$$\|R^{m+1} f\|^2 \leq \epsilon^2 \|f\|^2 \tag{71}$$

then stop. Otherwise , $m = m + 1$ *and go to* 2.

$\nu \in (0, 1]$ is the optimality factor and ϵ the error. The above algorithm is implemented, using an adaptation of Donoho's Wavelab Software (available at `//http:www-erl.mit.edi/~felix/Software` and http://www-stat.stanford.edu/~donoho/).

5.8 (De)-composition and time-frequency behavior

Fig. 8 contains an example of the (de)-composition and subsequent reconstruction (cf. Eq. 72) of an artificial signal (generated with the same dictionary as used for the decomposition) containing 3 "events". Comparison is made between an order/direction adapted (left column) and conventional non-adapted Wavelet Packet Dictionary (right). As we can see the adapted dictionary is able to decompose f in a fewer number of atoms, while the time-frequency plane is better resolved. Evidently, this improvement is the result of using a Wavelet Packet Dictionary, which is specifically designed to optimally represent the type of event in the data. As we know from multifractal analysis and from the results presented in this report (Sections 4 and 6), these events "look like" fractional derivatives of some bump function. Fractional Spline Wavelet Packet Dictionaries contain exactly the same type of events with the only difference; the decay rate for the high frequencies, i.e. the wavelet's regularity, varies with the wavelet order, maintaining a Hölder regularity that equals α. For the low frequencies the wavelets depart with a powerlaw $\alpha + 1$.

From the analysis in section 4 we learned that for positive α transitions, the order of the wavelet ($\beta = \alpha + 1$ for Fractional Spline Wavelets) has to exceed the order of the singularity. At the critical differentiation (with abuse in notation) when $\alpha = \alpha + 1$ we know that we are creating a local maximum, i.e. detecting the singularity. It is not clear how this property carries over to the correlation type of measure, underlying the Matching Pursuit search algorithm. Still, we may hope to expect the correlation measure to be large when the regularity of the smoothing function matches the regularity of the smoothed positive Hölder transition.

For negative order singularities in the data (read reflection data instead of well-log data), the story is quite different. In that case we expect the data to consist of smoothed fractional derivatives for which the correlation measure should be maximum in case the "wavelet" atom within the Fractional Spline Dictionary matches the position, scale, order and direction of the (seismic) event.

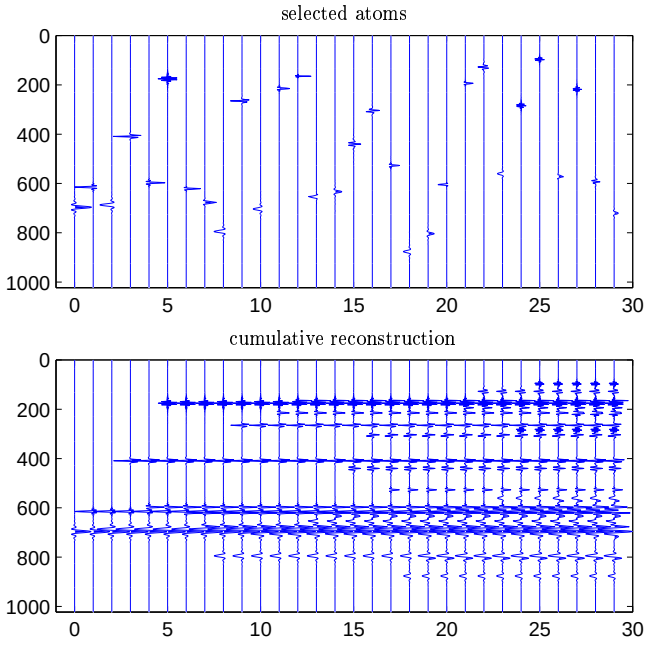

Figure 9: Example of a partial ($\#\alpha = 30$) atomic (de)-compostion of a seismic trace with $\alpha \in [0., 4]$ and $\sigma = 2^j$ with $j = 0 \cdots 5$. Top: the atomic decomposition (cf. Eq.'s 68-71). Bottom: the cummulative reconstruction. (cf. Eq. 72)

In any case since we constructed a very redundant dictionary by combining the different Fractional Spline Wavelet Packet Bases, we should expect an optimal decomposition, fined-tuned to the events in the data. Depending on the purpose of the decomposition, data compression *versus* singularity characterization, we can decide to use the whole depth of the tree or to limit the tree depth. In the first situation the algorithm tends to select oscillatory coarse scale atoms, which do not look like "natural" reflection events, whereas in the second situation the algorithm selects a variety of different order/direction atoms that match closely the individual reflection events in the data.

Fig. 9 illustrates the ($M = \#atoms = 30$) (de)-composition for a seismic trace with $N = 2^{10}$ samples and the depth of the tree set to $D = 5$, the scale $\sigma = 2^j$ with $j = 1 \cdots 5$. The composition is computed with

$$f_M(z) = \sum_{m=0}^{M} \langle R^m f, g_{\gamma_m} \rangle g_{\gamma_m}. \tag{72}$$

For a typical seismic data set (see e.g. Fig's. 10-12), the relative error is relatively small for $M = 50$ atoms and with a dictionary consisting of $\#\alpha = 50$, $\alpha \in [0, 4]$ directional Fractional Spline Wavelets. This relatively small number of atoms corresponds to a significant compression.

5.9 Compression and convergence properties: an empirical study

Fig's 10-12 contain examples of the atomic decomposition scheme applied to the traces of a seismic line. The number of atoms was set to $M = 100$ and $\alpha \in [0, 4]$ taking 50 different values in all three directions. The seismic line is depicted in Fig. 10 and is taken from the Jeanne d'Arc dataset. This dataset is also discussed by William Lyons (see this report), who attemps to make inferences on the litho-stratigraphical information content from the scale attributes computed with the method described in section 4 (see also section 6). As we can see from Fig.'s 11 and 12, the reconstruction is very good except for the very low and very high frequencies. The high frequency difference is mostly white and corresponds to differences between the atoms in the dictionary and the individual reflection events. To the eye there is not a lot of lateral coherency within these high frequencies. For the low frequencies, however, we do find coherent

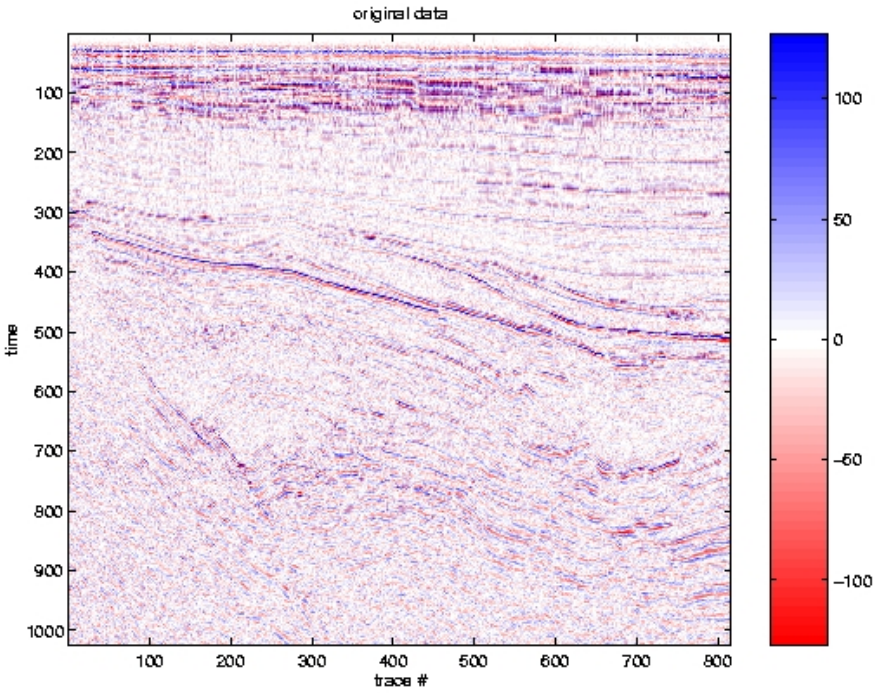

Figure 10: Line from the Jeanne d'Arc dataset.

structures. This low frequency content of the error can easily be reduced by stepping deeper into the tree ($D = 7$ in this case while total depth of the tree was 10).

As the above example shows we get a very reasonable reconstruction for $M = 100$, leading to tenfold compression rate that can even be improved by efficiently storing the atoms, which consist of a single real and integer valued index. Remains interesting to see what the convergence rate is of these scheme as compared to original schemes, consisting of only one Wavelet Packet Basis.

As stated earlier, there excists an extensive body of literature on asymptotic convergence results for non-linear approxations. For data with positive order singularities these results state that the convergence rates do not depend on the regularity/number of vanishing moments of the wavelet as long as the latter number exceed the Hölder regularity of the signal. However, these results are asymptotic and as one can see from the examples in Fig 8, we can gain quite a bit in compression when adopting the wavelet order and direction. In addition, we are able to estimate the order and direction (see also discussion below in section 6).

Finally, according to Mallat (1997) one can show that, for data with positive Hölder exponents, the error

$$\varepsilon = \|f - f_M\|, \tag{73}$$

converges to zero as $M \to \infty$.

5.10 Denoising

Depending on the choice of dictionary, the Matching Pursuit Algorithm finds coherent structures in the data with properties that closely match the atoms in the dictionary. This property allows us to optimally design the dictionary. Extending the original Wavelet Packet Dictionary to a dictionary with a multitude of different order Fractional Spline Wavelets, represents an optimal design, given the obsevation that well-log and seismic data are multifractal, i.e. contain a multitude of different order (coarse-grained) singularities.

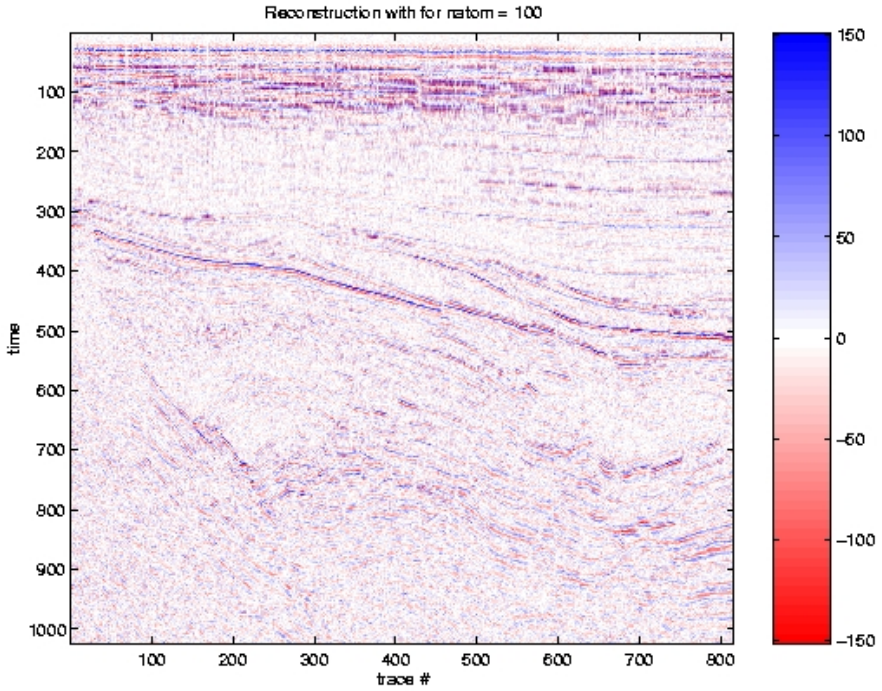

Figure 11: Reconstruction of the line depicted in Fig. 10 with $M = 100$ and $\alpha \in [0, 4]$ taking 50 different values in all three directions.

As described by Mallat (1997), the Matching Pursuit behaves like a non-linear chaotic map. For particular dictionaries, the normalized residues, $\frac{R^m f}{\|R^m f\|}$ converge to an attractor. This attractor corresponds to part of the signal that does not correlate well with the atoms in the dictionary. As the Matching Pursuit Algorithm progresses, more and more coherent structures are extracted from the data as to approximate f from a possible additive background noise, i.e. from $Z = f + W$, where Z is the noisy data and W the noise. Coherent structures are defined as atoms whose inner product with the noisy data exceeds the noise level. Given the noise level we are able to define an additional stop criterion for the Matching Pursuit Algorithm as described in Procedure 5.1. This stop criterion says that we stop as soon as the vector g_γ is no longer a coherent structure, i.e. if

$$\frac{|\langle R^m Z, g_{\gamma_m}|}{\|R^m Z\|} \leq S, \tag{74}$$

where S is the noise level. The denoised approximation of f can now be found as f_M (cf. Eq. 73) for which M is the minimal value yielding vectors g_γ that are still coherent structures. The estimator for the denoised f reads

$$\tilde{f} = \sum_{m=0}^{M} \langle R^m Z, g_{\gamma_m} \rangle g_{\gamma_m}. \tag{75}$$

Going back to Fig. 12 we can see that, for $M = 100$, we almost reached the level where additional atoms end up in the noise, i.e. become noise.

5.11 Deconvolution

As we have seen in Section 4, seismic reflectivity can, to leading order, be writen as a smoothed derivative of the variations in the earth elastic properties. The differentiation stems from the definition of the reflection density (cf. Eq. 3) itself and from additional differentiations invoked by the seismic wavelet

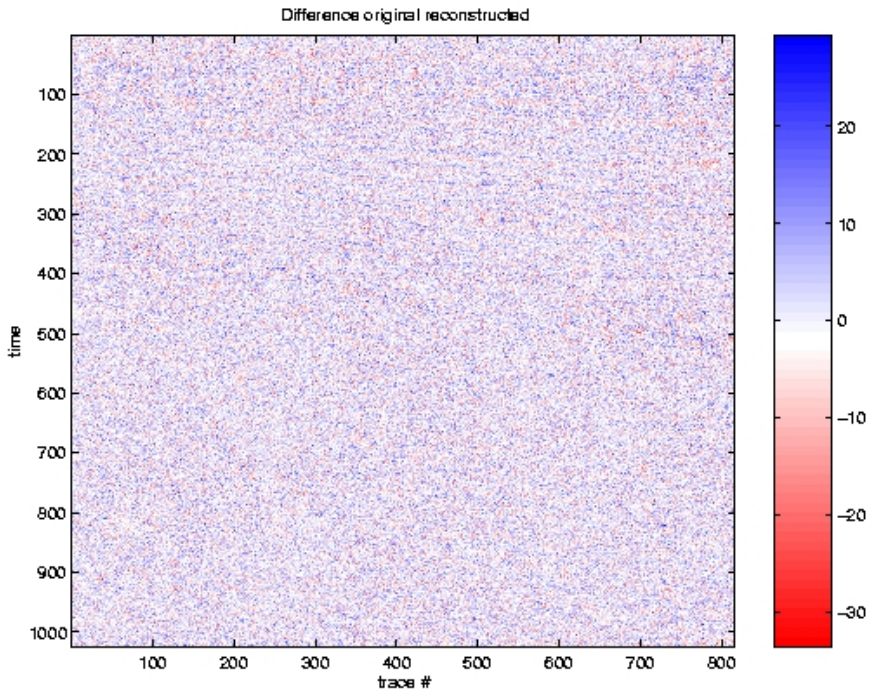

Figure 12: Differences between the original and reconstruction depicted in Fig'e 10-11, respectively. For the high frequencies there is very low coherence. For the very low frequencies there is coherence, which can be reduced by stepping deeper into the tree.

(seismic wavelets are bandwidth limited which implies that they entail some sort of derivative). For instance, in case of a Ricker/Mexican hat wavelet the total amount of differentiation equals $3 = 1 + 2$.

By changing the order of the atoms *prior* to reconstruction (cf. Eq. 72), we are able to remove the additional differentiation. Moreover, we may explore the tree structure of the Wavelet packet Basis by filling in the "blanks", i.e. stochasticaly interpolating the missing large and small scales using the estimated regularity. This approach is to some extent also followed by Neelamani et al. (2001) and H. Choi and Kingsbury (2000). We hope to report on future progress on this issue. For linear regularity adapted deconvolution and interpolation refer to Kane and Herrmann in this report.

5.12 Scale attribute extraction

Besides the compression and denoising capabilities of atomic decompositions, the atoms provide useful information on the litho-stratigraphical information content of data. As a result of the regularity and direction adaptation, the atoms not only provide information on the magnitude, location and characteristic dyadic scale of the events (the indices of the conventional wavelet packets) but also on the local coarse-grained Hölder regularity and directions of the transitions.

For bandwidth limited data, the estimated atoms lend themselves well for interpretation as we can see from the examples below. For well-log data, this is not necessarily the case because we will find atoms that reside on many different length scales. Moreover, the atoms are not limited to "details" (wavelets) only. The atoms also consist of "smoothings" for which it is not yet clear which inferences we can make about the largest inner product criterion.

5.13 Application to seismology

In this section we will review a number of examples of Atomic Decompositions of well-logs and their asociated reflectivity. For a more detailed discussion on attribute estimation, refer to section 6 and Lyon's contribution to this report.

5.14 Application to well-log data

In Fig. 13 we show an example of the atomic decompositon of a smoothed real well-log measurement. The $M = 100$, $\alpha = (-0.5, 2]$ and $\#\alpha = 50$ for the three directions. As we can see the smoothed well-log data is very nicely reconstructed (green line) by the composition. The first atoms in the decomposition have not been plotted because they correspond to the very low frequency components of the well-log. Unfortunately, not all atoms provide a clear insight in the different types of transitions. They merely constitute vectors that optimally represent the data. Besides, the afore mentioned problem with positive Hölder regular data, we are also dealing with a dataset in which there is still a lot of multiscale information present, which makes it difficult for the algorithm to find the transitions that are easily interpretable.

Fig. 15 contains the extracted attributes obtained from the atomic decompositions of several smoothings of the well-log measurement. The colorbar denotes the orders. The dyadic scale is given by the size of the colored symbols. The upper triangle is reserved for causal, the lower triangle for anticausal and the circle for symmetric. We can see that the estimates are relatively perisistent across different scales. The locations, however, are less well resolved as compared to the method described in section 4. Moreover, one can see that "red" attributes are found at the major jumps in the data, whereas "blue" attributes are located at regions where the well-log data display sharp peaks or troughs.

5.15 Application to seismic data

Before applying the atomic decomposition to real imaged reflection data, we first discuss an example with smoothed synthetic reflectivity, directly obtained from the well-log measurement depicted in Fig. 13.From, this example we can see that there is a reasonable consistency across the different scales. A similar observation applies to the estimated directions and orders.

To test our mehtod further, we plot part of the results after decomposing part of a line from the Jeanne D'Arc dataset. The results are presented in Fig. 16-18. From these Fig.'s we can see clearly that attribute analysis based on Atomic Decompositions is not as good as the *modulus maxima* method in finding the locations of the singularities. However, the method excels in characterizing the singularities rigorously.

Finally, we compare in Fig. 19 the time-frequency characteristics of conventional and Fractional Spline Atomic Decompositions of a trace of imaged reflection data. Clearly, the time-frequency localization of the Fractional Spline Wavelet Packets is superior to the non-regularity adapted conventional Wavelet Packet Basis.

6 Litho-Stratigraphical Facies Characterization

In this section, we present a case study on the relationship between the atom's attributes and possible litho-stratigraphical information content. Where possible we will compare the methods described in Sections 4 and 5. First, we start by introducing a Facies characterization for lithological boundaries, followed by a discussion on the Mobil AVO dataset. Central questions we ask ourselves are: (i) can we enhance the stratigraphy; (ii) is there lithlogical information in the sharpness and direction of the transitions; (iii) how do the attributes perform in relation to well synthetics. Lyons and Herrmann, address similar questions in their contribution to this report.

6.1 Facies transition categorization

Following Harms and Tackenberg (1972) we propose three simplified models for lithologic boundaries. The boundaries are related to contrast in the sand/mud ratio. As the sand content increases so does the velocity. The three facies types under consideration are (1) coarsening upwards, where the contact is a transition from fine-grained sediments below to coarser sediments above (see Fig. 20, top); (2) fining upwards, where the contact is a transition from coarse-grained sediments below to finer sediments above (see Fig. 20, middle), and (3) *symmetric* lobe shape sequences.

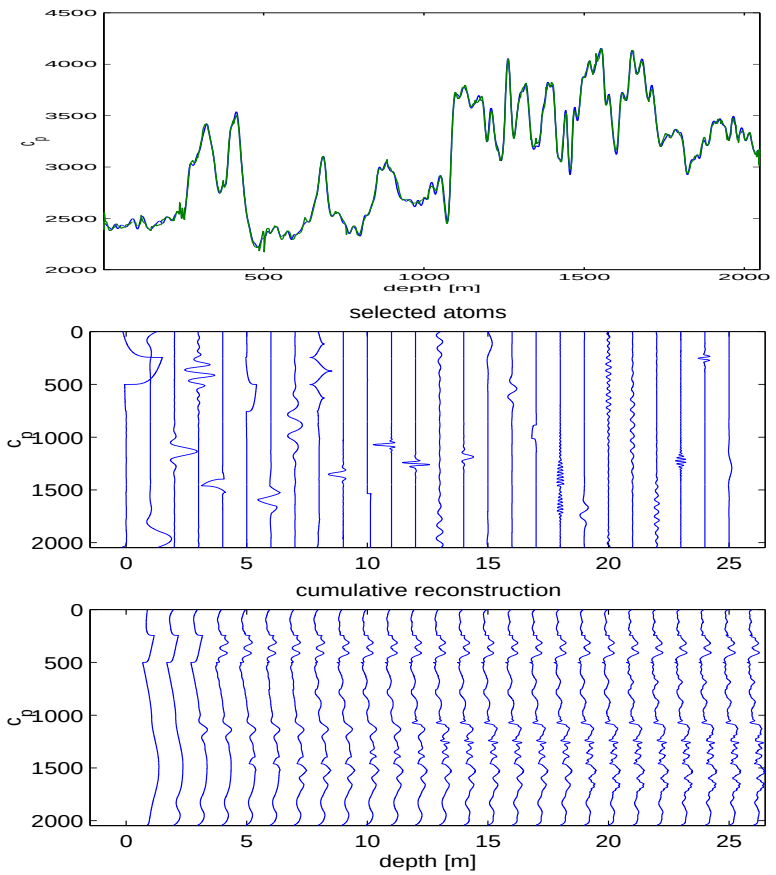

Figure 13: Atomic decomposition of a smoothed reall well-log with $M = 100$, $\alpha = (-0.5, 2]$ and $\#\alpha = 50$ for the 3 directions. Notice that the reconstruction is very accurate, while not all atoms readily lend themselves for interpretation.

Onsets defined in Eq. 55 provide models for these three types of transition zones. Setting the sharpness to a negative value $-1 < \alpha < 0$, (a)symmetric profiles are generated with varying sharpness and with characteristics similar to the nearshore regressive and marine transgressive facies.

6.2 Data and results for the monoscale method

The monoscale analysis method is applied to SEG's Mobil AVO data set (Keys and Foster, 1998), which contain well-logs and seismic data. Two areas of the time-migrated section are examined. The first (Fig. 21) covers a relatively large area, whereas the second (Fig. 22) zooms in on an area around the location of Well B. At roughly 2.4 s two-way traveltime, the lower Cretaceous claystone starts (left) and progresses to 2.05 s (right). This major unconformity is clearly visible in the seismic data (Fig. 21). While the seismic amplitudes vary significantly along this unconformity, the estimated scale exponents remain relatively constant along the major part of the horizon. Even though the quality of the migrated data varies, the attribute is able to delineate the stratigraphy because the method assigns only one attribute per lithologic boundary.

After correction for the wavelet (see below for detail), the exponent equals approximately ($\hat{\alpha} = -0.2$), which shows that the onset of the Cretaceous is sharper then a jump. This observation is consistent with the first onset of an 'M'-shaped transition zone as observed in the sedimentary record (see the well-log in Fig 22 at $t = 2.44$ s).

The second part of the analysis focuses on an area directly surrounding Well B. The sediment packages in this area consist of the Maastrichtian/Paleocene (M/P) and Paleocene/Ecocene (P/E) transitions (Lovell, 1994), which are both coarsening upward sequences that resemble the onsets, as illustrated in

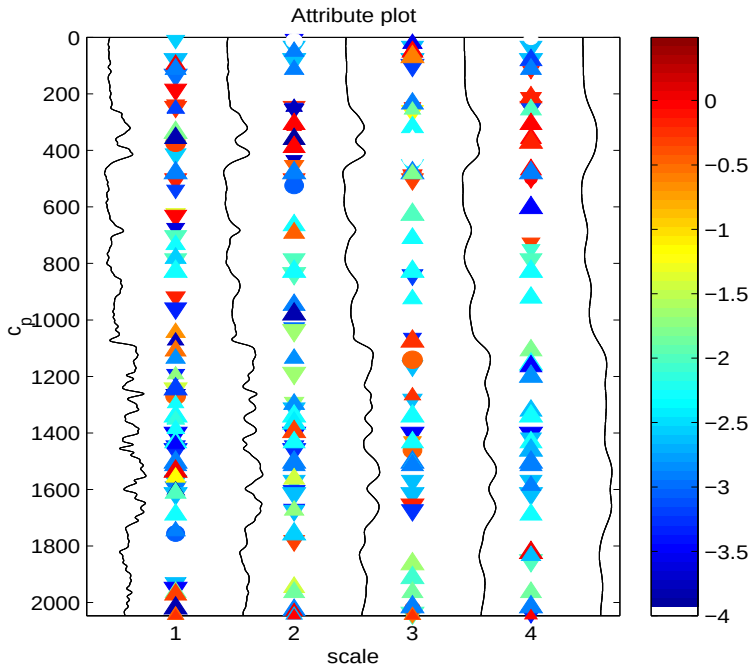

Figure 14: Attribute extraction for the atomic decompositions of different smoothings of well data. The colorbar refers to the orders, the triangle up means causal, triangle down anticausal and circle symmetric. Notice that the attribute estimates are reasonably stable across different scales.

Fig. 20. At both transitions, the sediment grain size increases up section to a maximum and then (relatively) rapidly decreases. However, the two horizons may be differentiated by the rate at which the maximum grain size is reached. Assuming the min/max grain sizes are roughly equal in each coarsening upwards cycle, the M/P rate of coarsening would be less than that of the P/E onset.

To confirm the above interpretation, the migrated data of Fig. 22 are analyzed by the monoscale analysis method. For reference the well is tied to the seismic data. Integrating the well and seismic data involves reflectivity modeling and wavelet estimation. The wavelet is estimated with a parametric inversion technique, minimizing differences between the modeled reflectivity and the neighboring migration amplitudes. The best fit corresponds to a wavelet order of $\gamma = 1.22$, yielding a parametrized wavelet close to the airgun's recorded source pulse (Keys and Foster, 1998).

As can be seen from the grey-scale plot in Fig. 22 there are still, despite detailed knowledge of both the well and seismic wavelet, significant differences between the modeled (middle of the section in Fig. 22) and measured amplitude values. These differences are very common and make it difficult to relate well data to seismic reflectivity on the level of amplitudes values. Therefore, we consider the scale attribute analysis as depicted by the color-coded dots in Fig. 22 as an alternative to the reflection amplitudes. The colored dots represent the location and sharpness of the reflection events. Agreement between results for the reflectivity from the well and the surrounding migrated data are superior to that of the amplitudes (grey-scale). There is lateral consistency (in location and singularity order) at a significant number of time horizons, since the attribute does not depend on the amplitude (only on the variations). Because the well data (using Eq. 6 with $\gamma = 1.22$ and s set to their parametric estimates) are directly converted into the synthetic reflectivity, we are able to compare the coarse grained Hölder exponents obtained from the well to those derived from the imaged seismic reflectivity.

In addition, singularity orders can be used to interpret lithology changes. For example, at $t = 2.05\,\mathrm{s}$ the method identifies a very sharp transition. Lithologically, this could be described as a thin sand layer within finer grained sediments. This finding is consistent with the lithologic interpretation of Lovell (1994). A second example, the singularity at $t = 1.79\,\mathrm{s}$, suggests a smoother lithologic transition. In the data this transition is interpreted as the top of the Paleocene sediments, which coarsen upwards. This coarsening is more gradual then the blocky sand, making the singularity analysis consistent with

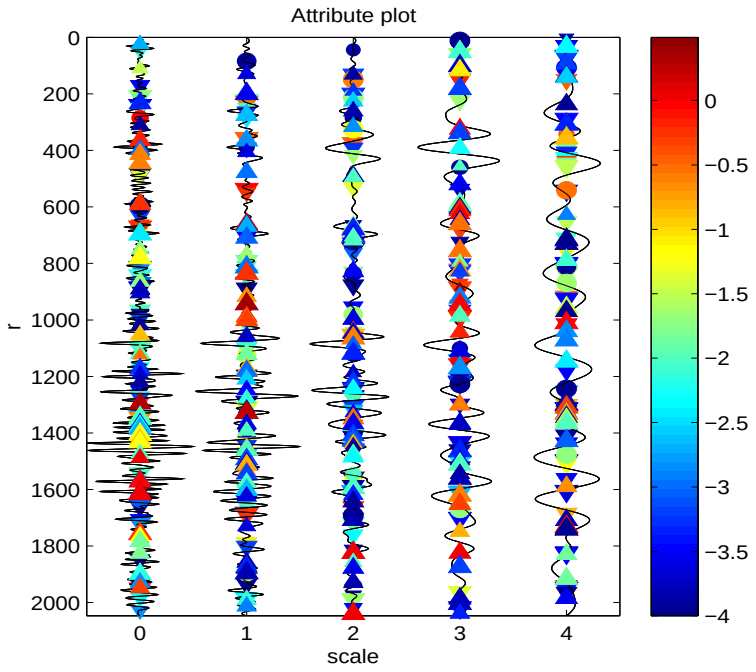

Figure 15: Attribute extraction for the atomic decompositions of different smoothed reflectivities computed directly from well data (see Fig. 15). The colorbar refers to the orders, the triangle up means causal, triangle down anticausal and circle symmetric. Notice that the attribute estimates are reasonably stable across different scales.

well-constrained lithology (Lovell, 1994). The observed consistencies demonstrate the usefulness of the quantification of lithologic transitions by singularity order.

6.3 Data and results for the Atomic Decomposition method

Besides the excellent reconstruction (see Fig's 10-12), the atom's parametrization (as we have seen in section 5.13) provides useful localized attribute information on the "amplitude", dyadic scale, order and direction of the reflectors. The amplitude measures the reflector strength and correlation reflection signature *versus* atom. The scale expresses the characteristic length scale, which is a function of the seismic wavelet and the length scale of the reflector. As the wave disperses the length scale increases. Contrary to scale, reflector order is *not* affected by dispersion because it reflects the low frequency behavior. However, the estimated order remains a relative measure because it contains a seismic wavelet contribution (e.g. an additional 2 for a Ricker wavelet). Finally, the direction information allows us to distinguish between (anti)-causal/symmetric transitions.

In particular, the order and direction (see Fig. 20) provide useful facies information. While the first attribute determines the transition sharpness which increases when changing from sand on sand to sand on mud for example (see also Lyons and Herrmann in these proceedings) and instantaneous phase behavior (Dessing, 1997), the direction enables us to distinguish between fining/coarsening upwards or lobe shape sequences.

As we can see from Fig.'s 23-24, the Atomic Decomposition yields attribute estimates whose location is not as well localized as within the monoscale method. Still, we find a lateral consistency of the attributes across the well at certain reflector horizons. In order to reduce the multiplicity, i.e. the assingment of multiple atoms at one and the same location, we only used the first $M = 50$ atoms. Fig. 24 is included to show a composite image of all estimated attributes. The color code for the attributes refers to the orders (blue sharp, red smooth), the size to the scale and the $\triangle$, $\triangledown$, $\circ$ to the directions.

At this point it is too early to draw definitive conclusions. Still, it is interesting to see how the attributes change along the major stratigraphical horizons.

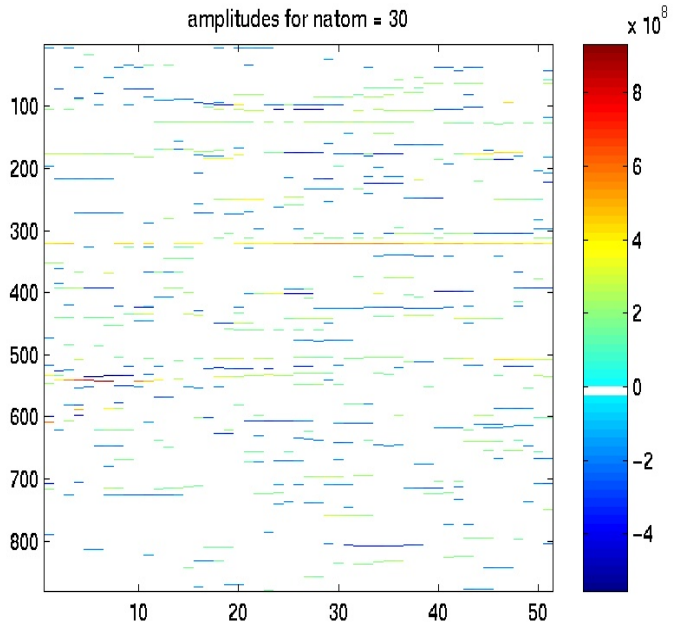

Figure 16: Example of the amplitude attribute plot obtained by the Atomic Decomposition with $M = 30$, $\alpha \in (0, 4]$, $\# = 25$ and all directions. The estimated amplitudes measure the strength of the signal and the correlation signal *versus* atom. Compared to the method described in section 4 the location of the singularities is not as well resolved. However, there is a clear lateral consistency although the amplitudes tend to vary significantly along the reflectors.

7 Discussion and conclusions

7.1 Monoscale method

In the first part of this paper, we presented a case where both the advantages and shortcomings of the continuous wavelet transform in seismology are revealed. Surely, as an analysis tool, wavelets are a natural analysis technique for seismological data because the wavelet transform is intrinsically linked to the physics of reflection seismology. Also, we show that seismic reflectivity to leading order behaves as a rescaled wavelet transform of the earth medium properties. Consequently, seismic waves share the property of triggering on singularities with wavelets, which opens the wavelet singularity characterization framework to seismology. When imaging is performed correctly, seismic processing is pseudo-differential, preserving the singularities, something which cannot necessarily be said about the seismic amplitudes. Therefore, introducing a singularity order map seems to be the appropriate way to infer information from seismic data, describing the earth's structure. As shown such a singularity map represents an image with localized information on the orders of magnitude of variations in the medium properties. These orders of magnitude are described by scale exponents, which capture the local regularity, local scaling and sharpness of the reflectors.

Besides the advantages of using the wavelet local regularity estimation framework, there is one important downside to wavelets — the bandwidth limitation of seismic data. As a result, seismic images contain information essentially residing at the fixed scale of the seismic wavelet. Clearly, this bandwidth limitation prevents successful application of the standard small-scale, asymptotic wavelet techniques. To overcome this fundamental difficulty, a monoscale analysis technique was presented which allows the estimation of coarse-grained local regularity estimates at the fixed scale. The method is based on a transform with respect to a family of integro-differentiations of the Gaussian bell-shape function, supplemented by two criteria. These two criteria predict the appearance or disappearance of modulus maxima as a function of the order of integro-differentiations for a special class of functions. The computational cost of this method is comparable to that of the ordinary scale asymptotic WTMML methods. The number of convo-

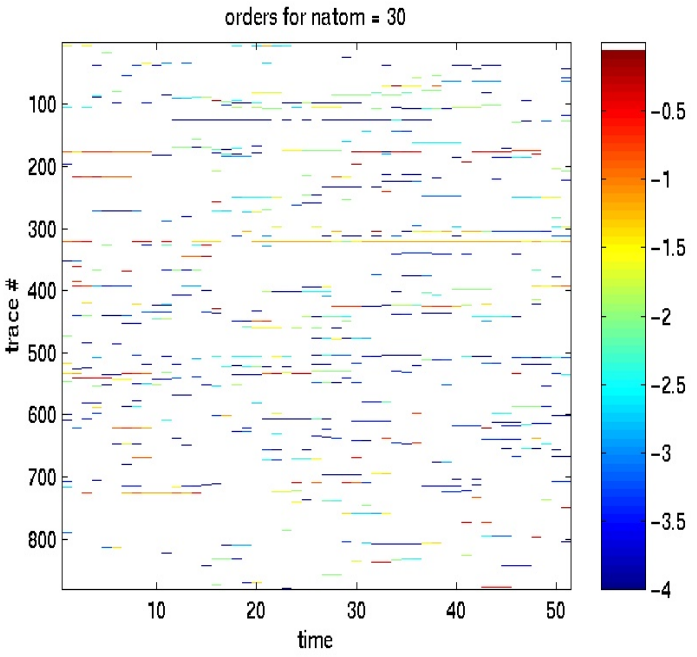

Figure 17: Example of the order attribute plot obtained by the Atomic Decomposition (see caption Fig. 16) The estimated orders measure the sharpness of the transitions which is related to the order of the best correlating atoms. Again we see a reasonable lateral consistency for the orders allthough the estimates do vary along the reflectors.

lutions and maxima searching are of the same order. However, compared to Struzik (2000)'s constraint local Hölder exponent estimation method, our approach has the advantage that it only assigns one single exponent per singularity. Because we limit the β-range, our method also automatically constrains the local slopes. Theoretically, there remain many issues to be resolved. For example, the directionality of the parametrized singularities is not easily resolved. Application of techniques from micro-local analysis may help to resolve this issue. Despite the lack of a formal theoretical justification of our method, the application of our transform and criteria to both well and seismic data demonstrate that singularity maps of well and seismic data do the following: (1) display heterogeneous scaling behavior, consistent with their observed multifractal behavior; (2) can be used to generate reconstructions; (3) can be used to interpret angle *versus* off-set behavior which, in part, is due to scaling; and (4) contain useful (geological) information on the location and local sharpness/regularity of the reflectors. Application of the essential one-dimensional monoscale analysis technique to seismic images shows a remarkable performance even though the data are two-dimensional.

7.2 Atomic decomposition

A new non-linear atomic decomposition method for seismic data is presented. Besides the substantial data compression the Atomic Decompostion denoises while the atom's parametrization reveal the transition's properties. Changes in scale, order, and direction of the atoms provide local information on lithological changes.

So far we have not been able to fully test the methodology. Results do, however, look promissing even though the method has its difficulties finding a lateraly consistent, i.e. stratigraphy consistent, characterization. Possible causes of this shortcoming are (i) the lack of shift invariance of the Wavelet Packet Bases (the shifts increase dyadically as we move to coarser scales); and (ii) the presence of local maxima in the correlation measure. The latter point corresponds to the possibility that there exist several atoms whose correlation only slightly differs, leaving room for "unwanted" differing atom assignments from trace to trace. Extension to higher dimensional Atomic Decompositions, based on truely multi-

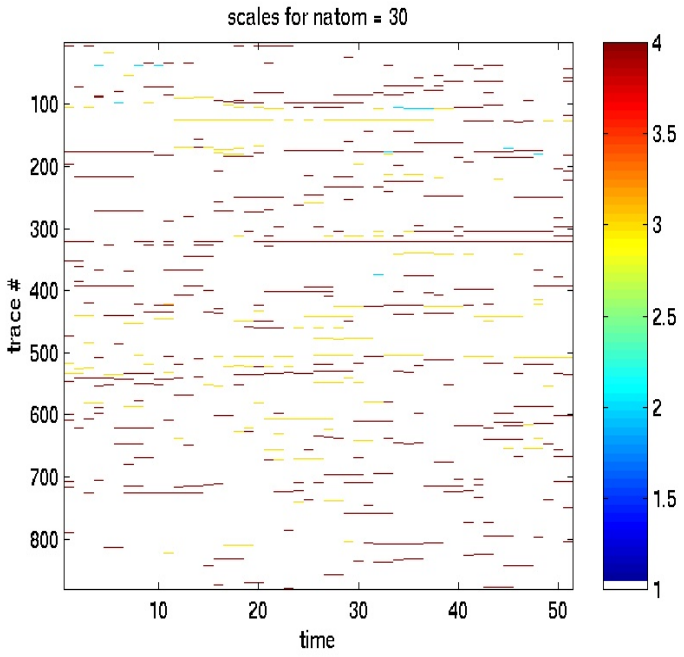

Figure 18: Example of the dyadic scale attribute plot obtained by the Atomic Decomposition (see caption Fig. 17). The estimated scales measure the composite effect of the characteristic length scale of the transitions and the length scale of the dispersive seismic wavelet. Again, we see a reasonable lateral consistency for the scales, although the estimates do vary along the reflectors.

dimensional basis functions (such as Curvelets, see e.g. Candès and Donoho (2001)) will hopefully resolve this important issue.

7.3 Facies characterization

Powerful new tools have been developed which allow for the introduction of a series of scale attributes. These attributes provide a *quantitative* seismo-stratigraphical description of the transitions from imaged reflection data. This description allows for improved geological interpretation of the stratigraphy and lithology. With the monoscale method the locations of the singularities are accurately estimated in a laterally consistent way, revealing a structural image.

Possible lithological changes along the major reflector horizons are expected to manifest themselves as attribute changes which can accurately be picked up by the Atomic Decomposition which not only provides information on the sharpness of the reflectors but also provides information on the amplitude, characteristic dyadic length scale, and direction. All these attributes describe the local texture, and therefore a possibility has been created to infer information on the depositional environment, underlying the litho-stratigraphy. Finally, the method faciliates the integration of well and seismic data.

Acknowledgements

This work was supported by the Industry Consortia at the Massachusetts Institute of Technology. I thank Colin Stark and Jeff Weissel for providing me with their unpublished manuscript regarding fractional order wavelets. Also I would like to thank Deilson M. Tavares for useful input. Finally, I thank the Troll unit members (Norkse Shell, Conoco Norge, TotalFinaElf, Statoil) for permission to publish their data.

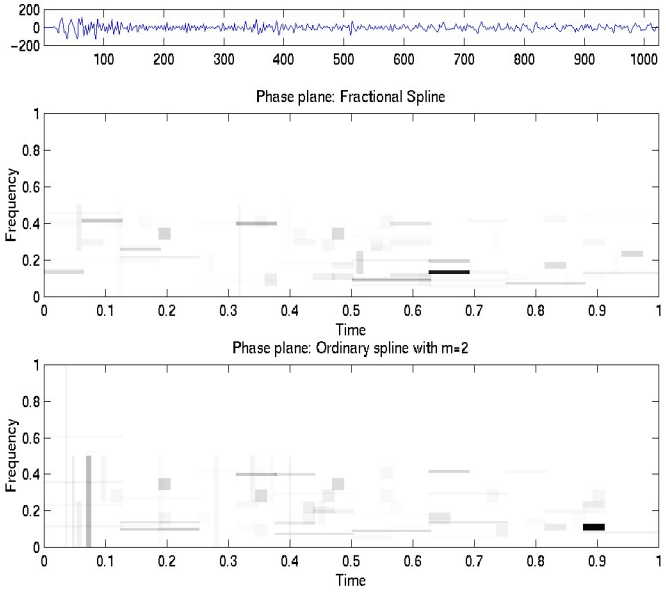

Figure 19: Comparison time-frequency characteristics. Top: reflectivity trace. Middle: Fractional Spline Atomic Decomposition. Bottom: Ordinary Wavelet Packet Decomposition. The atoms of the regulairy adapted Fractional Spline Decomposition are better localized.

References

E. Bacry, J. F. Muzy, and A. Arneodo. Singularity spectrum of fractal signals from wavelet analysis: Exact results. *Journal of Statistical Physics*, 70(3/4):635–674, 1993.

A. J. Berkhout. *Applied seismic wave theory*. Elsevier, Amsterdam, 1987.

Thierry Blu and Michael Unser. The fractional spline wavelet transform: Definition and implementation. In *Proceedings*, volume I, pages 512–515. IEEE, 2000.

Emmanual J. Candès and David L. Donoho. Recovering Edges in Ill-posed Problems: Optimality of Curvelet Frames. Technical report, Department of Statistics, Stanford University, 2001.

R. Carmona, W. Hwang, and B. Torrésani. *Practical time-frequency analysis*. Academic Press, 1998.

J. Catagna and M. Backus. *Offset-dependent reflectivity–Theory and practice of AVO analysis*. Soc. of Exploration Geophysicists, 1993.

R. R. Coifman, Y. Meyer, and V. Wickerhauser. Wavelet analysis and signal processing. In Ruskai et al. (1992), pages 453–470. 1992.

I. Daubechies. *Ten lectures on wavelets*. SIAM, Philadelphia, 1992.

M. de Hoop. Generalization of the bremmer coupling series. *Journal of Mathematical Physics*, 37(7): 3246–82, 1996.

M. de Hoop and N. Bleistein. Generalized radon transform inversions for reflectivity in anisotropic elastic media. *Inverse Problems*, 13(3):669–90, 1997.

M. V. de Hoop. *Directional decomposition of transient acoustic wave fields*. PhD thesis, Delft University of Technology, Delft, the Netherlands, 1992.

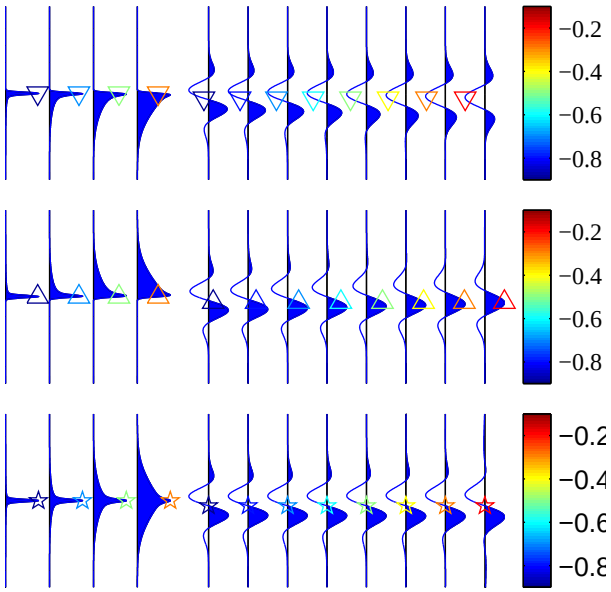

Figure 20: Generalization of onsets for geologic boundaries. Left column the causal (top), anti-causal (middle) onsets and symmetric (bottom) cusp as defined in Eq. 55 for $\alpha \in [-0.9, -0.1]$. The onsets model the coarsening upwards (top) and fining upwards (middle) lithologic and lobe shape (bottom) boundaries. As α increases the transition changes from a sharp, slightly skewed and smeared delta distribution to a less sharp jump discontinuity. The $\triangle$, ∇ and $\circ$ denote causal/anti-causal/symmetric and the order is color-coded (blue for sharp and red for less sharp). The reflection signatures (right column) for a Ricker wavelet (second derivative Gaussian) become more and more integrated as α increases. The colors for the reflections are corrected for the wavelet by $\alpha_{ref.} \mapsto \alpha_s + 2$, with the 2 corresponding to the amount of differentiation of the Ricker wavelet.

Martijn de Hoop. Direct, leading order asymptotic, inverse scattering based on the generalized bremmer series. In *Mathematical and Numerical Aspects of Wave Propagation*, pages 249–253. SIAM, 1998.

F. J. Dessing. *A wavelet transform approach to seismic processing.* PhD thesis, Delft University of Technology, Delft, the Netherlands, 1997. `http://wwwak.tn.tudelft.nl/~frankd`.

D. Emery and K. Meyers. *Sequence Stratigraphy.* Blackwell Science Publications Inc., 1996.

G. H. F. Gardner, editor. Society Of Exploration Geophysicists, 1985.

I. M. Gel'fand and G. E. Shilov. *Generalized functions*, volume 1. Academic press, 1964.

R. Gorenflo. *Fractals and Fractional Calculus in Continuum Mechanics*, chapter Fractional Calculus. Springer Verlag, 1997.

J. L. T. Grimbergen, F. J. Dessing, K. Wapenaar, and S. Kostek. Modal expansion of one-way operators in laterally varying media. *Geophysics*, 63(03):995–1005, 1998.

R.G. Baraniuk H. Choi, J. K. Romberg and N. G. Kingsbury. Hidden markov tree modeling of complex wavelet transforms. In *Proceedings of IEEE International Conference on Acoustics, Speech and Signal Processing - ICASSP'00*, 2000.

J. Harms and P. Tackenberg. Seismic signatures of sedimentation models. *Geophysics*, 37(1):45–58, 1972.

Felix Herrmann. Global texture characterization from well- and seismic data. 2000. to be submitted 01/02.

Felix Herrmann. Singularity Characterization by Monoscale Analysis: Application to Seismic Imaging. *Appl. Comput. Harmon. Anal.*, 2001. to appear March/June 2001.

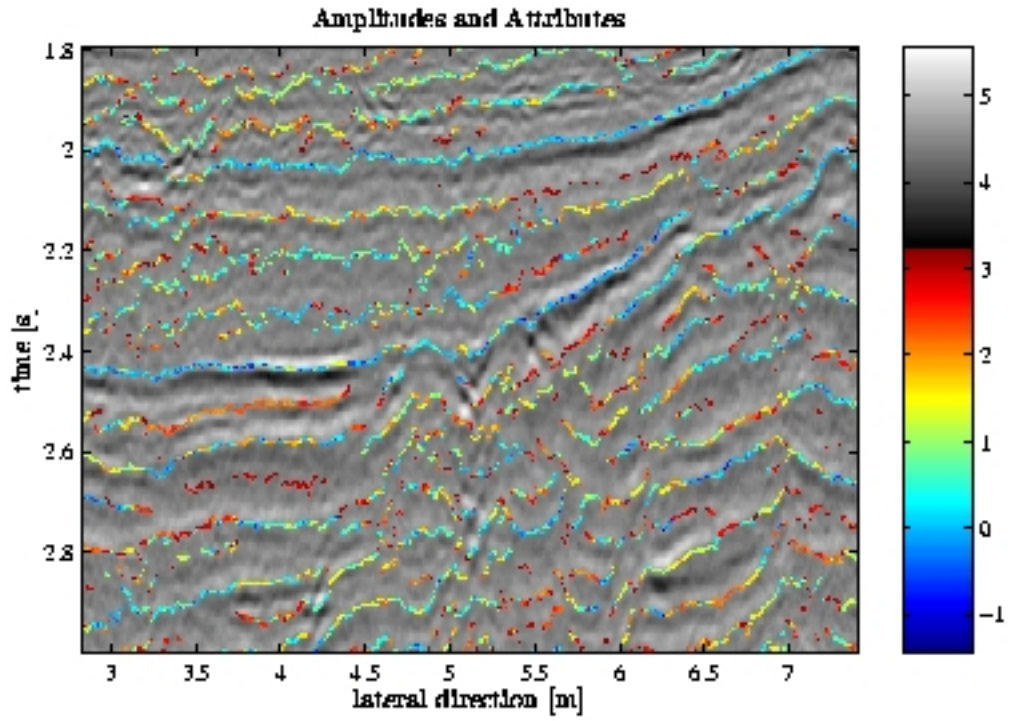

Figure 21: Selection of the time migrated Mobil dataset (Keys and Foster, 1998). Normalized seismic amplitudes in grey-scale and sharpness attribute in color-coded dots (blue and red again refer to sharp and less sharp). Both the position and order of the reflectors are recovered. The singularity structure aligns perfectly with the migration amplitudes variations. Lateral consistency along the reflectors is improved, e.g. along the onset of the lower Cretaceous (starts at $t = 2.4\,\mathrm{s}$ (left) and ends at $t = 2.0\,\mathrm{s}$).

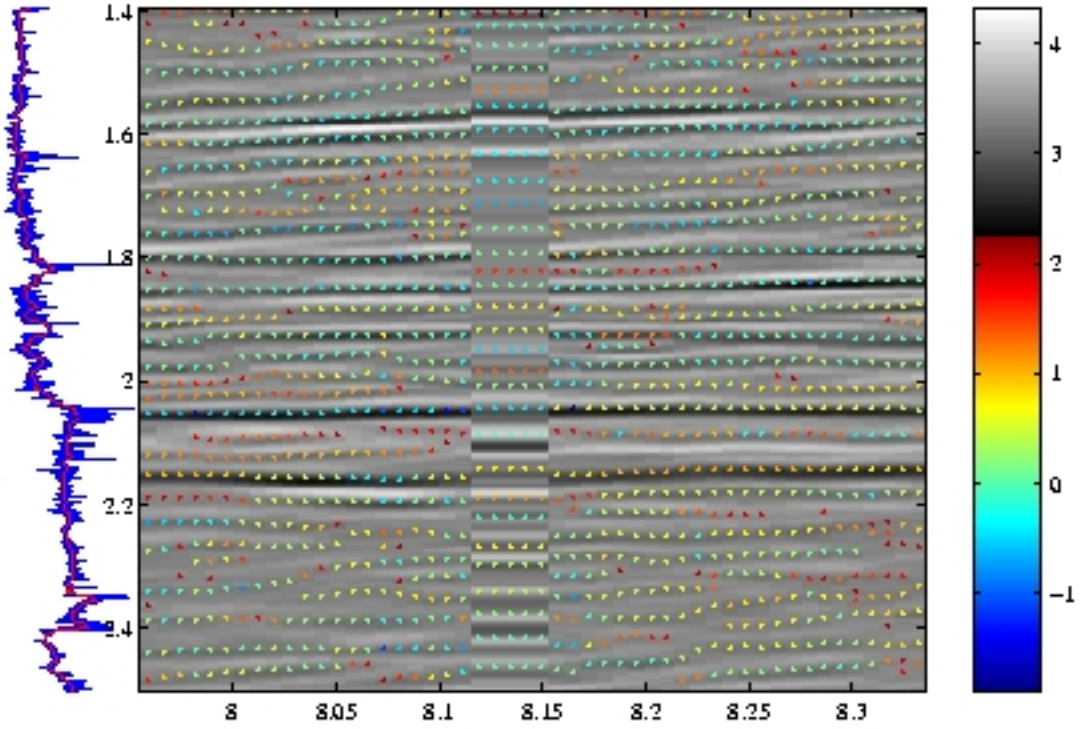

Figure 22: Well (left), migrated section (right) with tie in the middle. The well contains the acoustic impedances of the sedimentary record at the fine-grained well-log (blue) and coarse-grained seismic scale (red). Normalized migration amplitudes are in grey-scale and the sharpness attributes in colored dots. The tied well is located in the middle. Relating well to seismic data proves to be difficult for the grey-scale amplitudes. Despite some timing errors, the sharpness characterization (color code) integrates better across the well, while providing useful geologic information. Dots with colors close to red should not be emphasized since they either correspond to very smooth transitions or to artifacts. Finally, note that the 'M'-shaped unconformity should be located at a late time, as indicated by the check shots (Keys and Foster, 1998).

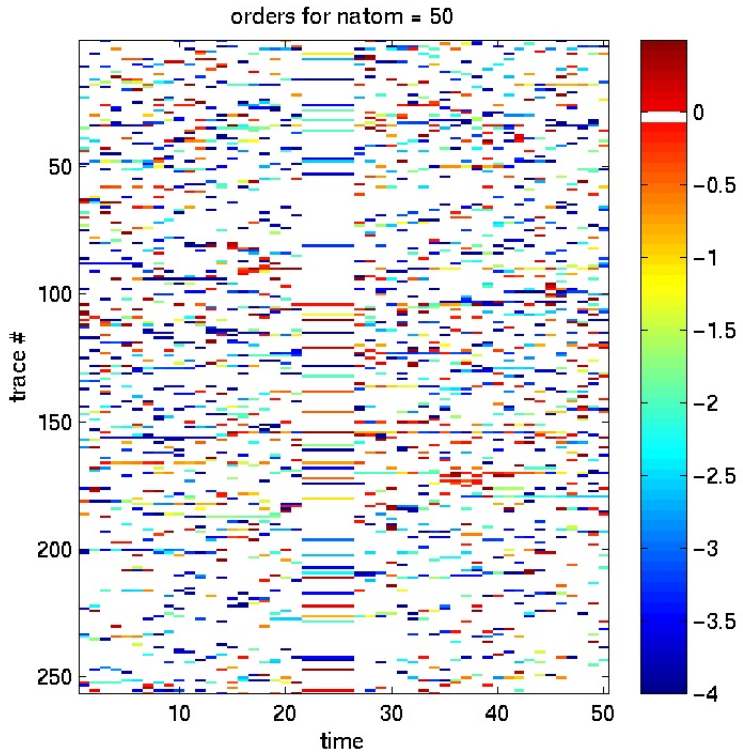

Figure 23: Order attribute for the migrated section included in Fig. 22, obtained from the Atomic Decomposition.

Felix Herrmann, Sebastien Chevrot, and Colin Stark. Sharpness characterization of the 410 upper mantle discontinuity by fixed scale singularity analysis of converted phases. *Geophysical Journal International*, 2000. submitted.

Felix Herrmann and Colin Stark. Monoscale analysis of edges/reflectors using fractional differentiations/integrations. In *Expanded Abstracts*, Tulsa, 1999. Soc. Expl. Geophys. `http://www-erl.mit.edu/~felix/Preprint/SEG99.ps.gz`.

Felix Herrmann and Colin Stark. A scale attribute for texture in well- and seismic data. In *Expanded Abstracts*, Tulsa, 2000. Soc. Expl. Geophys. `http://www-erl.mit.edu/~felix/Preprint/SEG00.ps.gz`.

Felix Herrmann and Colin Stark. Seismic facies characterization by monoscale analysis. 2001. submitted 6/00, `http://www-erl.mit.edu/~felix/Preprint/WellSeis.ps.gz`.

F.J. Herrmann. *A scaling medium representation, a discussion on well-logs, fractals and waves*. PhD thesis, Delft University of Technology, Delft, the Netherlands, 1997. `http://wwwak.tn.tudelft.nl/~felix`.

F.J. Herrmann. Evidence of scaling for acoustic waves in multiscale media and its possible implications. In *Expanded Abstracts*, Tulsa, 1998a. Soc. Expl. Geophys.

F.J. Herrmann. Multiscale analysis of well and seismic data. In Siamak Hassanzadeh, editor, *Mathematical Methods in Geophysical Imaging V*, volume 3453, pages 180–208. SPIE, 1998b.

M. Holschneider. *Wavelets an analysis tool*. Oxford Science Publications, 1995.

S. Jaffard. Multifractal formalism for functions part I: Results valid for all functions. *SIAM J. Mathematical Analysis*, 28(4):944–970, July 1997a.

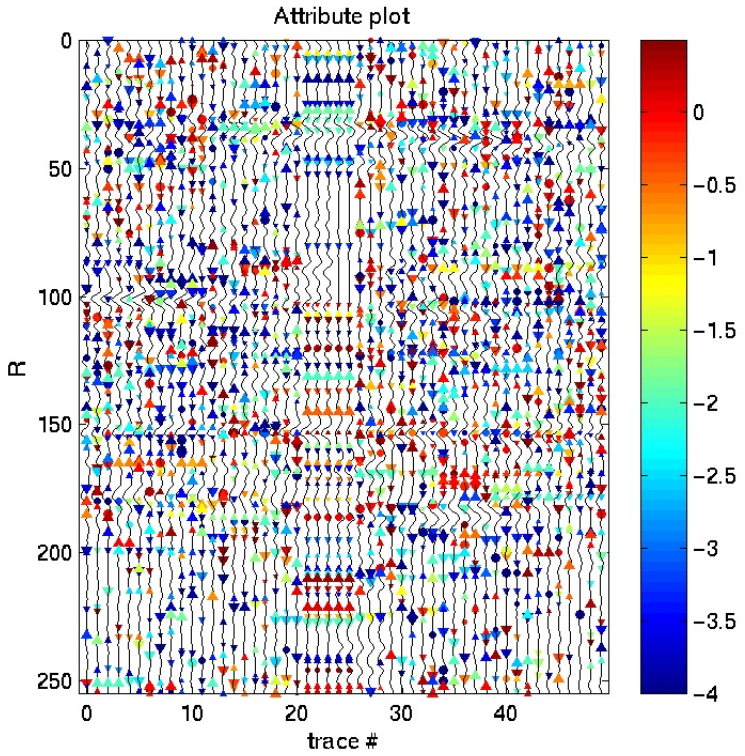

Figure 24: *Idem*, but now a composite plot with all the attributes.

S. Jaffard. Multifractal formalism for functions part II: Self-similar functions. *SIAM J. Mathematical Analysis*, 28(4):971–998, July 1997b.

S. Jaffard and Y. Meyer. *Wavelet Methods for Pointwise Regularity and Local Oscillations of Functions*, volume 123. American Mathematical Society, september 1996.

G. Kaiser. Wavelet filtering in the scale domain. volume 2825 of *SPIE Conference Proceedings*, August 1996.

Robert Keys and Douglas Foster. *Comparison of seismic inversion methods on a single real data set.* Society of Exploration Geophysicists, 1998.

J. Lovell. *Introduction to the petroleum geology of the North Sea.* Blackwell Scientific Publications, 1994.

Bill Lyons and Felix Herrmann. Lithologic characterization of stratigraphy by singularity analysis of seismic and well data. 2001.

S. G. Mallat. *A wavelet tour of signal processing.* Academic Press, 1997.

Stephane Mallat and Liang Hwang. Singularity detection and processing with wavelets. *IEEE Transactions on Information Theory*, 38(2):617–642, 1992.

J. Muller, I. Bokn, and J. L. McCauley. Multifractal analysis of petrophysical data. *Ann. Geophysicae*, 10:735–761, 1992.

R. Neelamani, J.K. Romberg, H. Choi, R. Riedi, and R. G. Baraniu. Multiscale Image Segmentation Using Joint Texture and Shape Analysis. Proceedings of Wavelet Applications in Signal and Image Processing VIII. SPIE, 2001.

W. Ostrander. Plane-wave reflection coefficients for gas sands at nonnormal angles of incidence. *Geophysics*, 49:1637–1648, 1994.

Charles Payton, editor. *Seismic stratigraphy – applications to hydrocarbon exploration*, chapter Stratigraphic models from seismic data. AAPG, 1977.

R. Riedi, M. Crouse, V. Ribeiro, and G. Baraniuk. A multifractal wavelet model with application to network traffic. *IEEE Transactions on Information Theory*, 1998.

M. B. Ruskai, G. Beylkin, R. Coifman, I. Daubechies, S. Mallat, Y. Meyer, and L. Raphael, editors. *Wavelets and their Applications*. Jones and Bartlett, 1992.

A. Saucier and J. Muller. Use of multifractal analysis in the characterization of geological formation. *Fractals*, 1(3):617–628, 1993.

Z. R. Struzik. Determining Local Singularity Strengths and their Spectra with the Wavelet Transform. *Fractals*, 8(2), June 2000.

W. W. Symes. Mathematics of reflection seismology. Technical report, The Rice inversion project, Rice University, 1995.

Michael Unser and Thierry Blu. Fractional splines and wavelets. *SIAM Review*, 42(1):43–67, 2000.

A.J. van Wijngaarden. *Imaging and characterization of angle-dependend seismic reflection data*. PhD thesis, Delft University of Technology, 1998.

Frederic Verhelst. *Integration of seismic data with well-log data*. PhD thesis, Delft University of Technology, 2000.

C. P. A. Wapenaar. One-way representation of seismic data. *Geophysical Journal International*, 178: 178–188, 1996.

C. P. A. Wapenaar and A. J. Berkhout. *Elastic wavefield extrapolation*. Elsevier, 1989.

Kees Wapenaar, Aart-Jan van Wijngaarden, and Wim van Geloven. Apparent AVA effects of fine-layering. *Geophsyics*, 64(6):1939–1948, 1999.

M. Zähle. Fractional Differentiation in the Self–Affine Case: V-The Local Degree of Differentiability. *Math. Nachr.*, 1995.

A. H. Zemanian. *Distribution theory and transform analysis; an introduction to generalized functions, with applications*. McGraw-Hill, New York, 1965.